

# ADVANCED FUNCTIONAL MATERIALS

## Supporting Information

for *Adv. Funct. Mater.*, DOI: 10.1002/adfm.202005594

Impact of Tin Fluoride Additive on the Properties of Mixed Tin-Lead Iodide Perovskite Semiconductors

*Kimberley J. Savill, Aleksander M. Ulatowski, Michael D. Farrar, Michael B. Johnston, Henry J. Snaith, and Laura M. Herz\**

**Supporting Information:**

**Impact of tin fluoride additive on the properties  
of mixed tin-lead iodide perovskite  
semiconductors**

Kimberley J. Savill, Aleksander M. Ulatowski, Michael D. Farrar, Michael B.  
Johnston, Henry J. Snaith, and Laura M. Herz\*

*Department of Physics, University of Oxford, Clarendon Laboratory, Parks Road, Oxford  
OX1 3PU, U.K.*

E-mail: [laura.herz@physics.ox.ac.uk](mailto:laura.herz@physics.ox.ac.uk)

# Contents

<b>1</b>	<b>Further experimental details</b>	<b>S-3</b>
1.1	Solution preparation . . . . .	S-3
<b>2</b>	<b>Structural characterisation by X-ray diffraction</b>	<b>S-3</b>
2.1	Identifying impurity peaks . . . . .	S-3
2.2	Calculating expected perovskite peak positions . . . . .	S-5
2.3	Influence of tin fraction and SnF <sub>2</sub> additive on crystal structure . . . . .	S-9
<b>3</b>	<b>Terahertz transmission through photoexcited films</b>	<b>S-14</b>
3.1	Sample thickness used in terahertz conductivity analysis . . . . .	S-15
<b>4</b>	<b>Analysis of dark conductivity spectra</b>	<b>S-15</b>
<b>5</b>	<b>Photoluminescence lifetime analysis</b>	<b>S-19</b>
<b>6</b>	<b>Analysis of absorbance spectra</b>	<b>S-24</b>
6.1	Determining bandgap . . . . .	S-26
6.2	Bandgap bowing fits . . . . .	S-27
<b>7</b>	<b>Analysis of photoluminescence spectra</b>	<b>S-30</b>
7.1	Details of spectral response correction . . . . .	S-30
7.2	Trends in PL peak position . . . . .	S-33
<b>8</b>	<b>Calculating charge-carrier mobility from OPTP measurements</b>	<b>S-37</b>
<b>9</b>	<b>Fitting empirical relationship between mobility and doping density</b>	<b>S-39</b>
	<b>References</b>	<b>S-40</b>

# 1 Further experimental details

## 1.1 Solution preparation

**Solution preparation** Two parent solutions (both 1.2 Molar) were prepared as described in Section 4 of the main text, and then mixed in the manner detailed in Table S1 to give a precursor solution for each of the desired Sn fractions. Different  $\text{FA}_{0.83}\text{Cs}_{0.17}\text{SnI}_3$  solutions were prepared for each  $\text{SnF}_2$  percentage, with 0, 0.1, 1, 5, 10, or 20 mol%  $\text{SnF}_2$  added relative to the tin content of this parent solution.

Table S1: Volumes of each precursor solution used to prepare  $\text{FA}_{0.83}\text{Cs}_{0.17}\text{Sn}_x\text{Pb}_{1-x}\text{I}_3$  films with varying tin fraction,  $x$ . Note that as samples at  $x = 0$  are prepared with none of the tin precursor solution to which  $\text{SnF}_2$  is added, the percentage of tin fluoride additive used for a given set of samples has no impact on the composition at  $x = 0$ , which always has an actual tin fluoride content of 0%.

Tin fraction	$\text{FA}_{0.83}\text{Cs}_{0.17}\text{PbI}_3$ ( $\mu\text{L}$ )	$\text{FA}_{0.83}\text{Cs}_{0.17}\text{SnI}_3$ ( $\mu\text{L}$ )
1	0	500
0.9	50	450
0.8	100	400
0.7	150	350
0.6	200	300
0.5	250	250
0.4	300	200
0.3	350	150
0.2	400	100
0.1	450	50
0	500	0

## 2 Structural characterisation by X-ray diffraction

### 2.1 Identifying impurity peaks

To assign the observed XRD peaks for  $\text{FA}_{0.83}\text{Cs}_{0.17}\text{Sn}_x\text{Pb}_{1-x}\text{I}_3$  samples, we first identify any non-perovskite peaks present by comparison with XRD patterns for the quartz substrate and any likely impurities. The XRD pattern for z-cut quartz was measured in the same way as

the perovskite samples, using a blank substrate, and data for the precursors used in sample fabrication were obtained from the literature as indicated in Table S2. Likely degradation products on exposure to oxygen and moisture were also considered, identifying SnO<sub>2</sub> and SnI<sub>4</sub> as the main possibilities not already covered by the precursor compounds,<sup>S1</sup> and so reference XRD data for these materials were also identified from the literature as shown in Table S2 for comparison to measured data.

Table S2: Literature sources for the XRD patterns of precursor materials and tin degradation products, as plotted in Figure S1.

<b>Material</b>	<b>Source for XRD pattern</b>
FAI	Petrov et. al., <i>Acta Crystallogr., Sect. E: Crystallogr. Commun.</i> , <b>2017</b> , 73, 569-572 <sup>S2</sup>
CsI	Aleksandrov, Goncharov, Makarenko and Stishov, <i>Phys. Rev. B</i> , <b>1991</b> , 43, 1990 <sup>S3</sup>
PbI <sub>2</sub>	Palosz, <i>J. Phys.: Condens. Matter</i> , <b>1990</b> , 2, 5285 <sup>S4</sup>
SnI <sub>2</sub>	Howie, Moser and Trevena, <i>Acta Crystallogr., Sect. B: Struct. Crystallogr. Cryst. Chem.</i> , <b>1972</b> , 28, 2965-2971 <sup>S5</sup>
SnF <sub>2</sub>	Denes, Pannetier, Lucas and Le Marouille, <i>J. Solid State Chem.</i> , <b>1979</b> , 28, 2965-2971 <sup>S6</sup>
SnI <sub>4</sub>	Reuter and Pawlak, <i>Z. Kristallogr. Cryst. Mater.</i> , <b>2001</b> , 216, 34-38 <sup>S7</sup>
SnO <sub>2</sub>	Yamanaka, Kurashima and Mimaki, <i>Z. Kristallogr. Cryst. Mater.</i> , <b>2000</b> , 215, 424-428 <sup>S8</sup>

Figure S1 shows these reference XRD patterns plotted with the measured data for FA<sub>0.83</sub>Cs<sub>0.17</sub>Sn<sub>x</sub>Pb<sub>1-x</sub>I<sub>3</sub> samples with varying tin fraction and different amounts of tin fluoride added to the tin precursor solution during preparation. The positions of significant peaks for the perovskite samples are marked with grey vertical lines for comparison to the possible impurity peaks, from which it can be seen that the four quartz peaks are present in each of the measured sample patterns, along with a weak lead iodide peak in the pattern for the neat lead perovskite sample, not seen for tin fractions greater than 0. The broad peak appearing for the neat tin perovskite sample with 0.1% SnF<sub>2</sub> near  $2\theta = 26^\circ$  can be assigned to tin fluoride, which has the most closely matched peak of the reference patterns. The other strong peaks in the perovskite XRD patterns are not well-matched by any of the likely impurities and so these are identified as originating from the perovskite, allowing peak

assignments based on probable crystal structure to be made as described in the following sections.

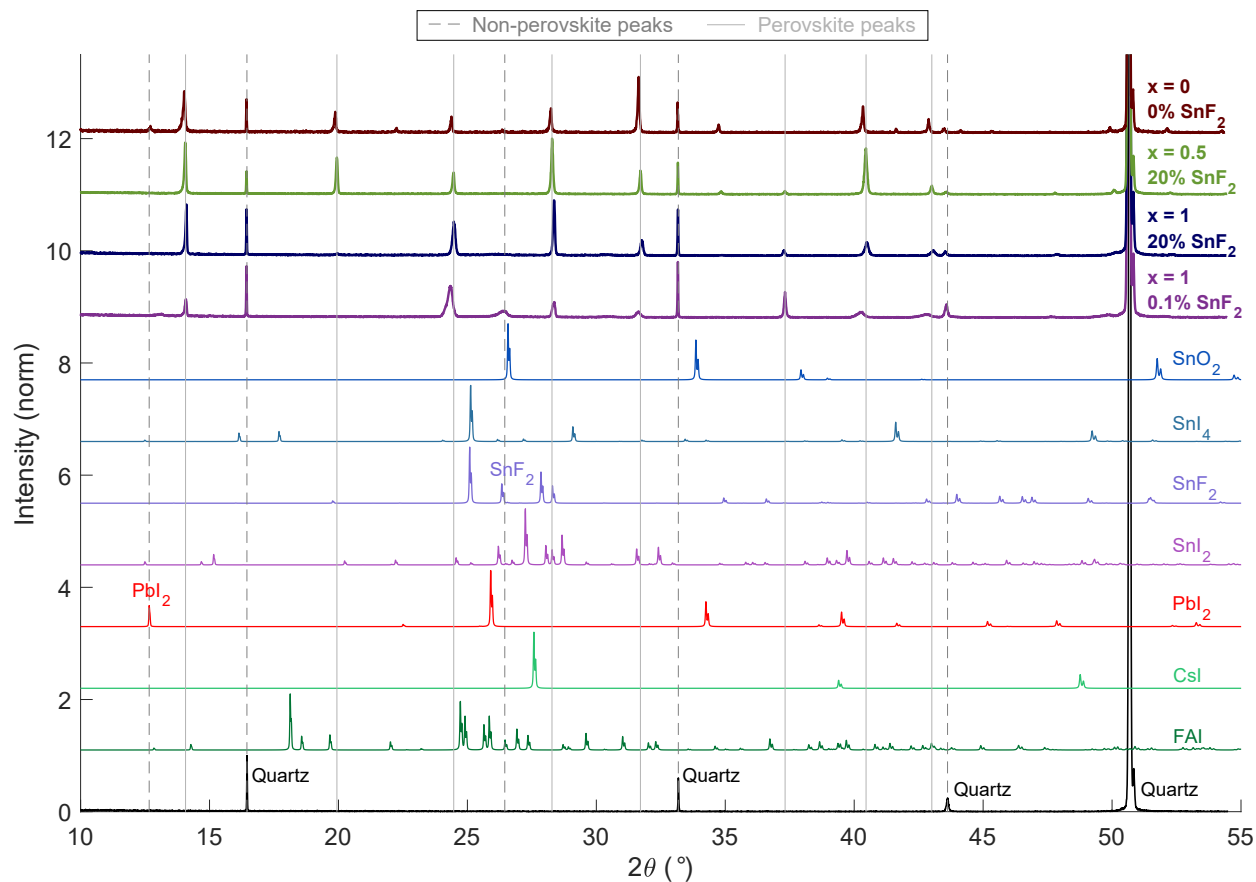


Figure S1: Comparison of measured XRD patterns against reference data for likely impurities. Measured XRD patterns for FA<sub>0.83</sub>Cs<sub>0.17</sub>Sn<sub>*x*</sub>Pb<sub>1-*x*</sub>I<sub>3</sub> thin films on z-cut quartz substrate are plotted with thick solid lines, labelled with tin fraction  $x$  and tin fluoride percentage added to the tin precursor solution during preparation. Reference XRD patterns for precursors and possible tin oxidation products as labelled are plotted with thin solid lines. Notable non-perovskite peaks in the measured diffraction patterns are marked with mid-grey dashed lines, while solid grey lines are used for the peaks identified as originating from the perovskite which do not have counterparts in any of the reference patterns. Reference XRD data were obtained from literature as specified in Table S2, and the pattern for z-cut quartz was measured directly using a blank substrate.

## 2.2 Calculating expected perovskite peak positions

To assign the XRD peaks identified as originating from the perovskite thin films, rather than any impurities, the crystal structure of the perovskite must be identified. In previous stud-

ies on tin-lead perovskites, their structure has often been identified as either (pseudo)cubic or tetragonal, noting tetragonal distortion varying with tin fraction<sup>S9-S11</sup> or cation substitution.<sup>S12</sup> We therefore consider these structures as the most likely when interpreting our measured XRD patterns.

Starting with the assumption that the crystal structure of  $\text{FA}_{0.83}\text{Cs}_{0.17}\text{Sn}_x\text{Pb}_{1-x}\text{I}_3$  can be described as pseudocubic, the position  $2\theta$  of expected diffraction peaks can be determined given the corresponding Miller indices  $hkl$ , the cubic lattice parameter  $a$  and the wavelength  $\lambda$  of the X-ray source according to Equation 1:

$$\sin^2 \theta = \frac{\lambda^2}{4a^2}(h^2 + k^2 + l^2) \quad (1)$$

By comparison with previously reported XRD patterns for related perovskites assigned as pseudocubic<sup>S10,S12</sup> the peak appearing in each of the measured XRD patterns near to 14 degrees (marked with a black \* in Figure S2) can be identified as the (100) peak for a cubic structure, which allows the value of  $a$  to be determined given the known value of  $\lambda = 15.40598$  nm for the Cu  $K\alpha_1$  line used as the source in these measurements. Table S3 shows the results of this calculation for the three samples for which measured XRD patterns are shown in Figure S2, spanning the range of tin fractions.

Table S3: Cubic lattice parameters calculated from measured XRD patterns according to Equation 1 for an example set of  $\text{FA}_{0.83}\text{Cs}_{0.17}\text{Sn}_x\text{Pb}_{1-x}\text{I}_3$  thin film samples across the range of tin fractions.

$\text{FA}_{0.83}\text{Cs}_{0.17}\text{Sn}_x\text{Pb}_{1-x}\text{I}_3$ sample	(100) peak $2\theta$ ( $^\circ$ )	$a$ (nm)
$x = 0$ , 0% $\text{SnF}_2$	14.029	63.077
$x = 0.5$ , 20% $\text{SnF}_2$	14.062	62.928
$x = 1$ , 20% $\text{SnF}_2$	14.096	62.780

The lattice parameter values determined in this way can then be used in Equation 1 to calculate the expected position of the other peaks in the XRD pattern for a cubic structure, for each (degenerate) set of Miller indices. The expected peak positions given by this calculation are shown by black lines below each of the XRD patterns in Figure S2. The calculated

peaks show fairly good agreement with the measured perovskite peaks, all of which have a corresponding peak predicted for the cubic crystal structure except for the peak appearing around 37 degrees at higher tin fractions.

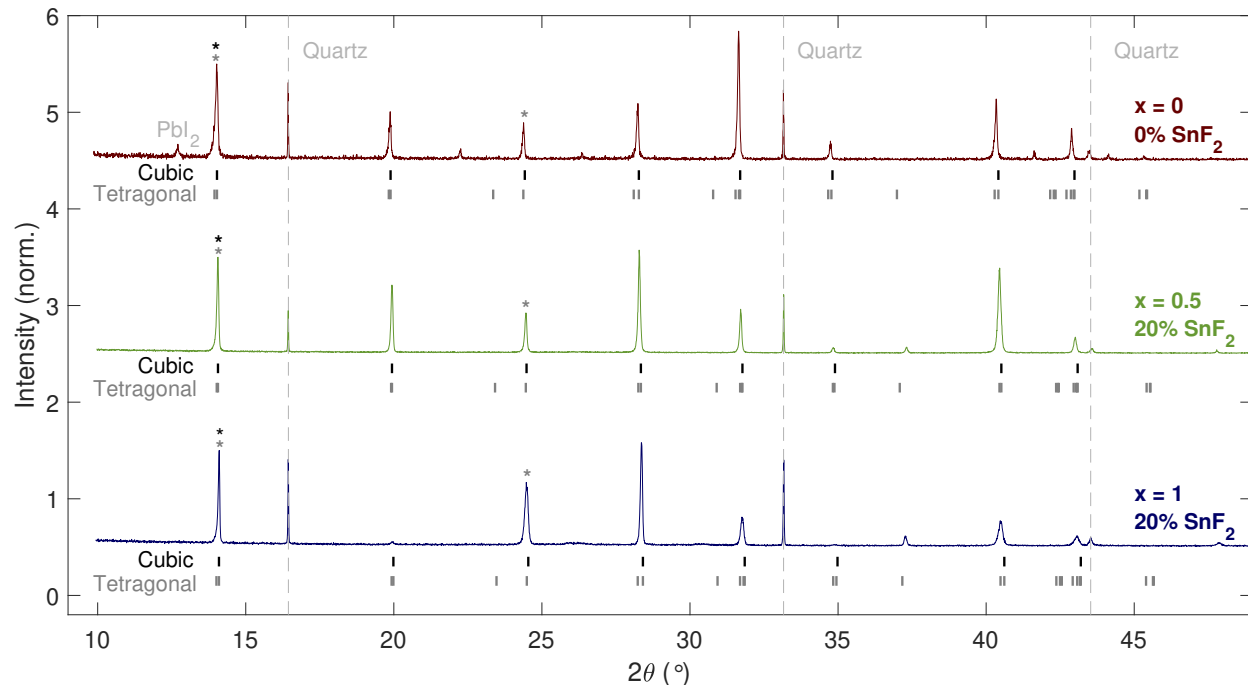


Figure S2: Measured XRD patterns of  $\text{FA}_{0.83}\text{Cs}_{0.17}\text{Sn}_x\text{Pb}_{1-x}\text{I}_3$  thin films on z-cut quartz substrate, for tin fractions and tin fluoride percentages as marked, with calculated peak positions assuming either cubic or tetragonal structure shown below each pattern in black and dark grey respectively. The measured peaks used to determine the lattice parameter/s for the calculated peak positions are marked by asterisks also in black or dark grey.

To explain the origin of this peak appearing near 37 degrees, which was not found to match any of the precursors or expected impurities (see Section 2.1) and is not expected for a cubic crystal structure, we consider the possibility of lower crystal symmetry. Moving from a cubic structure with a single lattice parameter  $a$ , to a tetragonal structure in which there is distortion along one axis requiring two lattice parameters  $a$  and  $c$  to describe the resulting lower symmetry unit cell, the equivalent relationship to that shown in Equation 1 is given by Equation 2.

$$\sin^2 \theta = \frac{\lambda^2}{4} \left( \frac{h^2 + k^2}{a^2} + \frac{l^2}{c^2} \right) \quad (2)$$

Predicting peak positions in the diffraction pattern for a tetragonal structure requires values of both lattice parameters to be determined. By comparison to the complete simulated XRD patterns for cubic and tetragonal MAPbI<sub>3</sub> given by Jacobsson et. al.<sup>S13</sup> we can identify the measured peaks near to 14° and 24° (marked with grey \* in Figure S2) as corresponding to tetragonal 110 and 022 peaks respectively, sufficient to determine both *a* and *c* by solving Equation 2 simultaneously for these two peaks in each pattern. The resulting lattice parameter values for the samples illustrated in Figure S2 are shown in Table S4.

Table S4: Tetragonal lattice parameters calculated from measured XRD patterns according to Equation 2 for an example set of FA<sub>0.83</sub>Cs<sub>0.17</sub>Sn<sub>*x*</sub>Pb<sub>1-*x*</sub>I<sub>3</sub> thin film samples across the range of tin fractions.

FA <sub>0.83</sub> Cs <sub>0.17</sub> Sn <sub><i>x</i></sub> Pb <sub>1-<i>x</i></sub> I <sub>3</sub> sample	(110) peak 2θ (°)	(022) peak 2θ (°)	<i>a</i> (nm)	<i>c</i> (nm)
<i>x</i> = 0, 0% SnF <sub>2</sub>	14.029	24.373	89.205	126.91
<i>x</i> = 0.5, 20% SnF <sub>2</sub>	14.062	24.457	88.994	126.23
<i>x</i> = 1, 20% SnF <sub>2</sub>	14.096	24.490	88.784	126.32

From the lattice parameters in Table S4 the position of each of the expected peaks in the XRD pattern for a tetragonal structure (having Miller indices which satisfy  $h + k + l = 2n$  for some integer *n*) can then be calculated from Equation 2. The results of this calculation are shown in Figure S2 by the grey markers for expected tetragonal peak positions plotted below the expected cubic peak positions for each of the XRD patterns shown. Comparing the predicted tetragonal peaks against the measured data, it is immediately apparent that as well as predicting peaks at all the observed positions which could be explained as cubic, the previously unexplained peak near 37° corresponds well to an expected peak for the tetragonal structure. The Miller indices of this peak are (231), which indicates that there is no lower-order diffraction peak which should be observed from the same set of crystal planes, so we can assign the 37° peak as originating from tetragonally structured perovskite and having indices (231).

Not all of the predicted tetragonal peaks are evident in the measured XRD patterns however: the 121 peak near 23.5°, the 123 peak near 31°, and the clusters of peaks around 42° do not have clear counterparts in the measured data, nor do the predicted peaks above

45°. These absences may indicate that the dominant structure is very close to cubic, but they could also be a result of preferential orientation of crystallites in the thin film samples. Such non-random orientation would prevent some diffraction peaks predicted for a powder with random orientations from being observed, although for each peak that is seen any lower or higher order diffraction peaks involving the same set of crystal planes should still be observed. In our data none of the absent tetragonal peaks has a corresponding lower or higher order diffraction peak appearing in the measured pattern, so this non-random orientation explanation is a possibility. As such, the existence of predicted tetragonal peaks which do not appear in the measured data does not contradict our assignment of the peak near 27° as the (231) tetragonal peak.

### **2.3 Influence of tin fraction and SnF<sub>2</sub> additive on crystal structure**

With significant peaks fully assigned for each of the measured XRD patterns, as shown by the labelling in Figures S3 and S4, we can analyse the trends seen with varying tin fraction or tin fluoride percentage to understand the effects of these compositional variations on the structure of the samples. Comparing the measured XRD patterns shown in Figures S3 for the full range of tin fractions with 0% or 20% SnF<sub>2</sub> added, and in Figure S4 for the full range of tin fluoride percentages at tin fraction 1, we identify three peaks of particular interest which are highlighted in Figure 1A of the main text. The lowest angle perovskite peak, with Miller indices (100) in the pseudocubic structure, is evident for all tin fractions and shows some variation in intensity with tin fluoride percentage as well as changing position with tin fraction. The pseudocubic (111) peak is similarly present for all measured samples (except FA<sub>0.83</sub>Cs<sub>0.17</sub>SnI<sub>3</sub> with 10% SnF<sub>2</sub> added, where crystallites are strongly oriented such that the XRD pattern plotted in green in Figure S4 shows the (100) and (200) peaks at far higher intensity than the quartz substrate peaks) and shows significant broadening for some compositions. Third, the peak assigned as tetragonal (231) which could not be accounted for assuming a pseudocubic structure appears correlated with tin fraction and

anti-correlated with tin fluoride percentage. This differs from the previously reported trend in  $\text{MASn}_x\text{Pb}_{1-x}\text{I}_3$  where a tetragonal structure for majority lead compositions changes to pseudocubic for tin fractions of 0.5 and above.<sup>S9–S11,S14</sup> The trends in intensity, position, and broadening of these three peaks are therefore interesting to explore in greater detail, as is done in Figure S5 and Figure 1 in the main text.

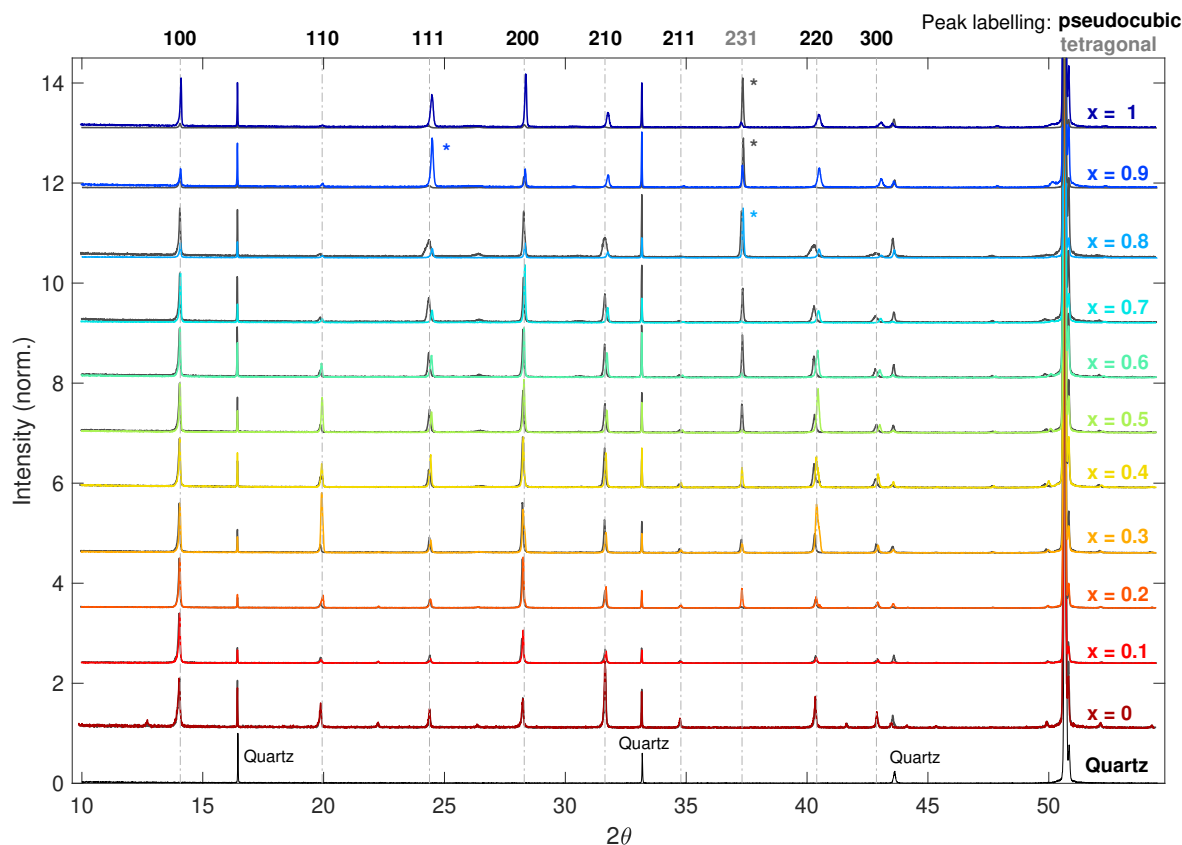


Figure S3: Measured XRD patterns for  $\text{FA}_{0.83}\text{Cs}_{0.17}\text{Sn}_x\text{P}_{x_{1-x}}\text{I}_3$  thin films on z-cut quartz substrate with tin fraction  $x$  ranging from 0 to 1 as labelled, and either 0% (dark grey lines) or 20%  $\text{SnF}_2$  (coloured lines) added to the tin precursor solution during preparation. All diffraction patterns have been normalised to the (100) peak (pseudocubic labelling) except for cases where another perovskite peak was much more intense and was therefore used to normalise to instead, indicated by an asterisk next to that peak in the corresponding colour. The colour scheme used here matches that used in Figure 1A in the main text where the (100), (111) and (231) peaks from these data are shown. The measured XRD pattern of a blank z-cut quartz substrate is also shown in black at the bottom of the figure.

The intensities for the three peaks of interest shown in Figure S5, determined by integrating over the peak in each case, illustrate that for the (100) and (111) peaks there is very

little variation in intensity with tin fluoride percentage or with tin fraction, the (111) peak being less intense for tin fraction 0 and 0.1 but only by around one order of magnitude. By contrast the tetragonal (231) peak is so weak as to be essentially absent for tin fractions 0 and 0.1, as can be seen by eye in panel A of the figure, and over the rest of the range there are variations in intensity with addition of tin fluoride. In general, for low tin fractions ( $x \leq 0.4$ ) the samples with tin fluoride added show a stronger (231) peak than the samples without any tin fluoride added while for higher tin fractions the addition of tin fluoride appears to suppress this peak, but the opposite behaviour is seen at  $x = 0.8$ . While differences in crystallite orientation throughout the sample can contribute to the relative intensity of peaks originating from diffraction with any given set of planes, the observed trends in intensity for the (231) peak suggest tetragonal distortion increases with increasing tin fraction, becoming particularly large for tin fractions 0.9 and 1, and can be reduced on addition of tin fluoride.

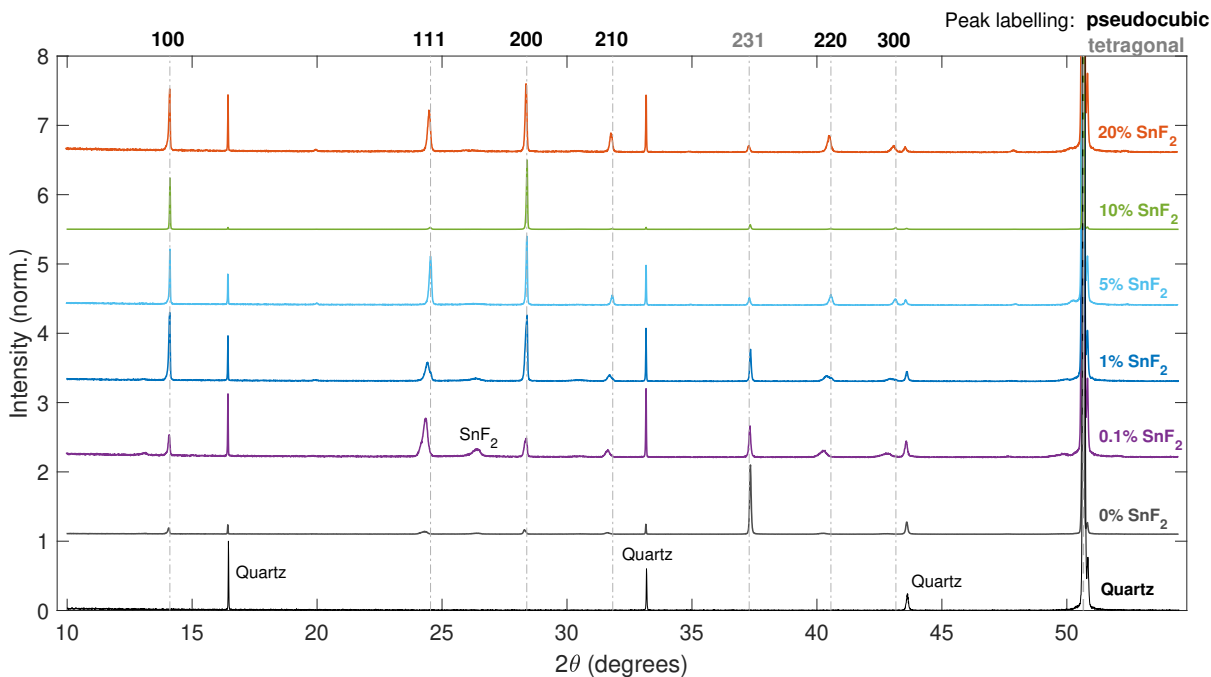


Figure S4: Measured XRD patterns for FA<sub>0.83</sub>CS<sub>0.17</sub>SnI<sub>3</sub> thin films on z-cut quartz substrate, with tin fluoride percentages ranging from 0% to 20% SnF<sub>2</sub> added to the tin precursor solution during preparation as labelled. For ease of display, each diffraction pattern has been normalised to the most intense peak occurring between 11 and 45 degrees. The measured XRD pattern of a blank z-cut quartz substrate is also shown in black at the bottom of the figure.

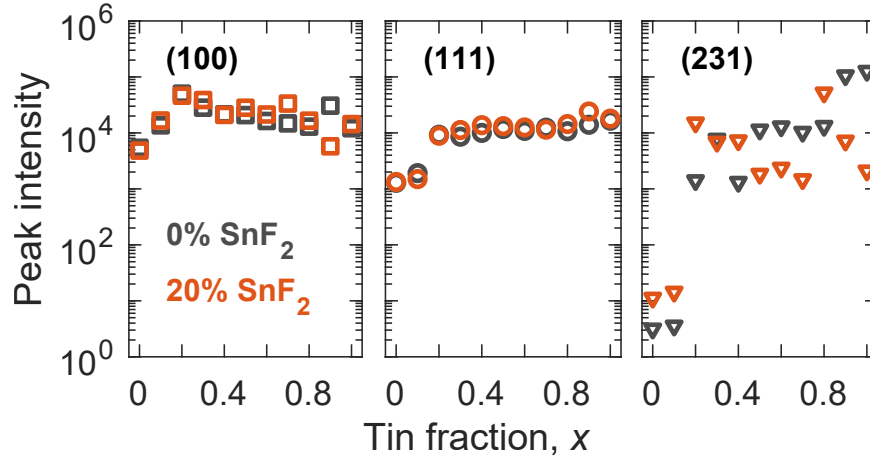


Figure S5: Effect of tin fraction and tin fluoride additive on the intensity of selected XRD peaks for  $\text{FA}_{0.83}\text{Cs}_{0.17}\text{Sn}_x\text{Pb}_{1-x}\text{I}_3$  thin films on quartz substrate with varying tin fraction and either 0% or 20%  $\text{SnF}_2$  added to the tin precursor solution during preparation. XRD patterns were measured with the  $\text{Cu-K}_\alpha$  line as incident radiation, and data are shown here for three peaks of interest: pseudocubic (100) and (111), and tetragonal (231), as marked. Peak intensity is calculated as the integral under each peak, and shows significant impact of  $\text{SnF}_2$  addition on the (231) peak in particular. Data for 0%  $\text{SnF}_2$  are shown in dark grey, and for 20%  $\text{SnF}_2$  in bright orange, as indicated. The markers and colour schemes used here match those used in Figure 1 of the main text, which shows the FWHM and peak position data for these three XRD peaks.

Considering the position and broadening of these three peaks, quantified in Figure 1 of the main text, together with the intensities just discussed provides further evidence for tetragonal distortion increasing with tin content and being suppressed by tin fluoride addition. The observed broadening of the (111) peak at high tin fractions, which is dramatically reduced by the addition of 20%  $\text{SnF}_2$ , is consistent with tetragonal distortion. For the tetragonal structure a second peak at lower angle is expected here, with greater separation from the observed pseudocubic peak than for most other splittings as illustrated in Figure S2, such that with lattice distortion along one axis significant broadening towards lower angle is to be expected for this peak in particular. We attribute the observed distortion away from pseudocubic crystal structure to the formation of tin vacancies which occurs along with hole doping when  $\text{Sn}^{2+}$  is oxidised.<sup>S15,S16</sup> The presence of these vacancies can induce strain in the lattice, which then distorts towards a lower symmetry structure.<sup>S17,S18</sup> The dominant pseu-

docubic structure observed with 20% SnF<sub>2</sub> is then explained by the role this additive plays in suppressing the oxidation of tin, thereby reducing the background hole doping density and the density of tin vacancies, resulting in a less distorted lattice structure. Similarly, for low tin fractions even without tin fluoride addition there can be relatively few tin vacancies relative to the B sites occupied by either Pb<sup>2+</sup> or Sn<sup>2+</sup> and so we do not observe a significant degree of tetragonal distortion for these compositions.

Figure S4 shows measured XRD patterns for the full range of tin fluoride percentages, added to samples with tin fraction 1, and illustrates similar trends which supports this explanation. The tetragonal (231) peak is the most intense in the measured pattern when no tin fluoride is added, decreasing progressively in intensity as tin fluoride percentage increases, and this change is accompanied by the (111) peak becoming less broadened and shifting to higher angle. Both of these observations are consistent with a reduction in tin vacancy-induced tetragonal distortion on addition of tin fluoride.

A further trend noticeable from the measured XRD data is that each of the peaks of interest shows a shift to higher angle as tin fraction increases, which is independent of tin fluoride addition except in the case of the (111) peak where broadening can mask the peak shift. This is to be expected given that the ionic radius of tin is smaller than that of lead and lattice parameters therefore shrink as tin fraction increases, as reflected in the calculated lattice parameters shown in Tables S3 and S4 for samples with tin fraction 0, 0.5, and 1. As can be seen from Equations 1 and 2, smaller lattice parameters correspond to larger values of  $\sin^2 \theta$  and therefore larger values of  $2\theta$ , giving the peak shifts observed. Similar changes in XRD peak position with tin fraction have previously been observed for tin-lead iodide perovskites with a range of organic cations.<sup>S10,S19,S20</sup> A small shift to higher angle with tin fluoride addition, as seen particularly clearly for the (100) peak, can be explained similarly with the presence of SnF<sub>2</sub> ensuring greater incorporation of Sn<sup>2+</sup> into the lattice.

### 3 Terahertz transmission through photoexcited films

Previous publications investigated the relation between the differential THz transmission signal (obtained from OPTP experiment) and the photoconductivity of thin films, by assuming a lack of conductivity of the reference sample (which is, in our case, the same film in the dark).<sup>S21,S22</sup> This leads to the following expression for photoconductivity (conductivity arising from photoexcited charge carriers),  $\sigma_{\text{photo}}$ , commonly used in literature:<sup>S23-S26</sup>

$$\sigma_{\text{photo}} = \left[ \frac{\epsilon_0 c (n_A + n_B)}{L} \right] \frac{\Delta T}{T} \quad (3)$$

where  $n_A = 1$  is the vacuum refractive index,  $n_B = n_{\text{quartz}} = 2.13$ <sup>S23</sup> is the refractive index of the substrate,  $L$  is the thickness of the sample and  $\Delta T/T$  is the ratio of the photoinduced change in THz transmission to the transmission through the sample in the dark.  $\epsilon_0$  and  $c$  are the permittivity of free space and the speed of light, respectively.

However, owing to the relatively high dark conductivity of tin-containing perovskites, reported in this publication, Equation 3 no longer holds, as its derivation assumes a lack of conductivity of the reference sample.<sup>S21</sup> We therefore used a modified equation, which accounts for the contribution of background electric doping:<sup>S27</sup>

$$\sigma_{\text{photo}} = \left[ \sigma_{\text{dark}} + \frac{\epsilon_0 c (n_A + n_B)}{L} \right] \frac{\Delta T}{T} \quad (4)$$

where  $\sigma_{\text{dark}}$  is the DC Drude conductivity of the sample without the photoexcitation.

In this study, Equation 4 was used to evaluate the photoconductivity, and hence mobility (see Section 8) of the electrically doped thin films, which required a measurement of dark conductivity to be performed for each sample as described in Section 4 below.

### 3.1 Sample thickness used in terahertz conductivity analysis

Film thickness  $L$  for the samples used in this study was determined by calculation according to Equation 5 from measured Napierian absorbance,  $A$ , (as shown in Figure S11) together with known absorption coefficient  $\alpha$  for perovskite thin films with equivalent composition measured previously.<sup>S28</sup>

$$\alpha = \frac{A}{L} \quad (5)$$

The mean value of film thickness calculated in this way for samples in this study was  $430 \pm 30$  nm. In terahertz conductivity analysis, specifically calculations for dark conductivity spectra as described in Section 4, a value of  $L = 400$  nm was used.

## 4 Analysis of dark conductivity spectra

Dark conductivity spectra of  $\text{FA}_{0.83}\text{Cs}_{0.17}\text{Sn}_x\text{Pb}_{1-x}\text{I}_3$  thin films were measured with the laser setup as described in Section 4 of the main text. The time-domain measurement of the transmitted THz radiation was conducted for each sample as well as for the bare quartz substrate, by changing the time delay between the THz beam and the gate beam. The time-dependent field strength of the THz pulse was then Fourier-transformed into frequency space and the dark conductivity spectra were calculated using:

$$\sigma_{\text{dark}}(\omega) = \left[ \frac{\epsilon_0 c (n_A + n_B)}{L} \right] \frac{T_{\text{quartz}}(\omega) - T_{\text{sample}}(\omega)}{T_{\text{sample}}(\omega)} \quad (6)$$

which is similar to Equation 3, but using the transmission through a bare, non-conductive quartz substrate as a reference.

The background hole densities (shown in Figures 3B and 5 in the main text) were obtained from the real part of the complex dark conductivity spectra, by using the Drude conductivity

model and assuming that the mobilities of electrons and holes are balanced<sup>S29</sup> ( $\mu_e = \mu_h = \frac{\mu}{2}$ ):

$$\sigma_{\text{dark}}(\omega) = \frac{\sigma_{\text{DC}}}{1 - i\omega\tau} = \frac{p_0 e \mu / 2}{1 - i\omega\tau} \quad (7)$$

where  $\sigma_{\text{DC}}$  is the DC conductivity limit ( $\omega \rightarrow 0$ ),  $\tau$  is the average scattering time of charge carriers, and  $p_0$  is the background hole density in the doped films.

Since the scattering time of charge carriers in metal halide perovskites was shown to be short compared to the THz oscillation period ( $\frac{1}{\tau} \gg \omega$ ),<sup>S25</sup> the real dark conductivity in the spectral region shown in Figures S6 and S7 here, and Figures 2 and 3A in the main text (0.5 – 2 THz) represents the DC conductivity of the samples, and, as indicated in Equation 7, its value is constant and equal to:

$$\Re[\sigma_{\text{dark}}(\omega < 2 \text{ THz})] = p_0 e \frac{\mu}{2} \quad (8)$$

Dark conductivity spectra, as calculated from Equation 6, encapsulate the sum of contributions from free charge carriers, as well as from the lattice response of the thin films. Due to prominent optical phonon features, present in the considered spectral range,<sup>S23</sup> we found it necessary to subtract the phonon contribution in order to extract the background hole doping density from Equation 8. This was done by using the dark conductivity spectra of the films with the highest SnF<sub>2</sub> content (20%), for which we note that suppression of the free charge carrier contribution (vertical offset of the spectrum) results in dark conductivity spectra dominated by the phonon response. These spectra are shown in Figure 2A in the main text as well as Figure S6.

Figure S7 shows the raw real dark conductivity spectra of FA<sub>0.83</sub>CS<sub>0.17</sub>Sn<sub>*x*</sub>Pb<sub>1-*x*</sub>I<sub>3</sub> thin films on the left, and the phonon response subtracted spectra on the right. The raw spectra exhibit features around 1 THz and 1.5 THz, which are caused by optical phonon modes of the lead/tin-iodide sub-lattice vibrations.<sup>S23</sup> We subtracted the spectrum of the 20% SnF<sub>2</sub> thin film in each sample set shown on the left in Figure S7 from the other spectra in the set, to

give the phonon response subtracted spectra shown on the right of that figure. For samples with low raw dark conductivity and larger measurement uncertainty (shown by the error bars in the panels on the left of the figure) conductivity values of spectra for which the phonon response has been subtracted are sometimes negative, but still within the uncertainty. We note that although for high tin fractions the addition of tin-fluoride significantly decreases the dark conductivity of the films (due to reduction of tin oxidation), this effect is no longer noticeable for lower tin fractions because the background hole density is much lower even without  $\text{SnF}_2$  addition.

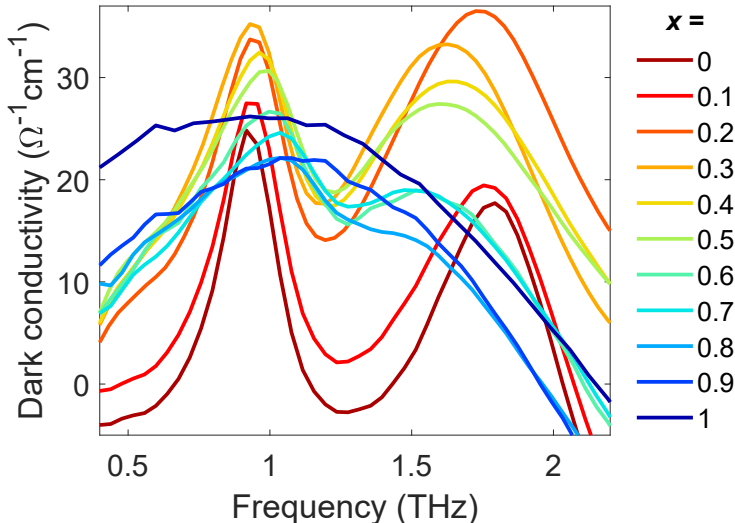


Figure S6: Response from lattice vibrations seen in dark conductivity spectra (real part) of  $\text{FA}_{0.83}\text{Cs}_{0.17}\text{Sn}_x\text{Pb}_{1-x}\text{I}_3$  thin films on z-cut quartz with tin fractions  $x$  as indicated in the legend, prepared with 20%  $\text{SnF}_2$  added to the tin precursor solution for each sample. The colour scheme used for tin percentage matches that used in Figure 2A of the main text where these spectra are shown with vertical offsets added, and the effect of phonon peak broadening and shift of the phonon response frequency are discussed. Here the spectra are directly overlaid to allow a direct comparison of the phonon response strength. We note that phase error due to differences in the thickness of the sample and reference substrates between measurements contributes to variations in peak intensity, with this effect being more pronounced at high frequency, as discussed by La-o-vorakiat et al.<sup>S30</sup>

To calculate the background hole density, the phonon response subtracted real dark conductivity spectra (shown in Figure S7 on the right) were used, together with Equation 8 and the mobility values obtained from OPTP measurement (as described in Section 8).

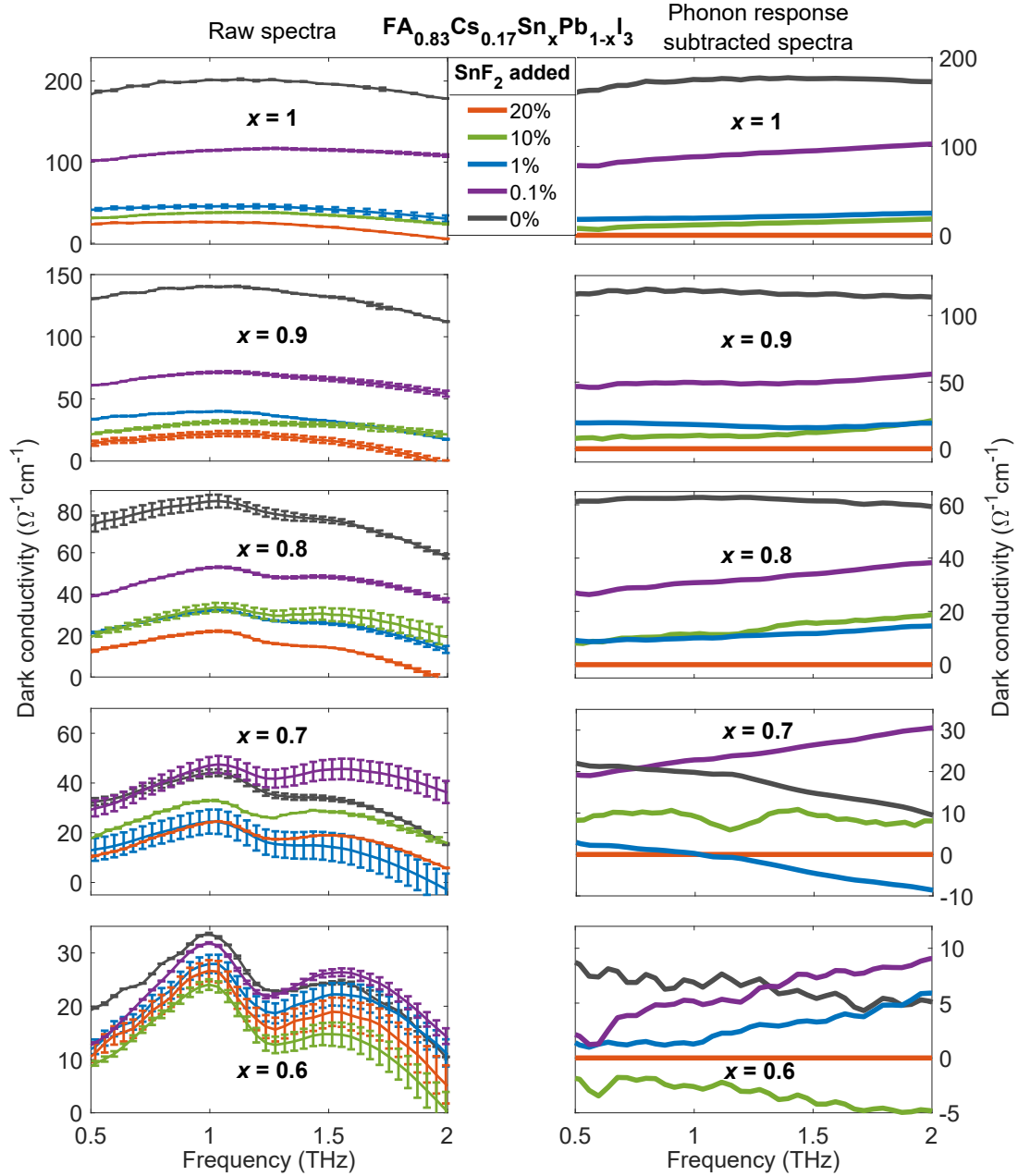


Figure S7: Raw real dark conductivity spectra (left) including both hole background conductivity from unintentional doping and optical phonon response, and dark hole conductivity spectra with phonon contribution subtracted (on the right) of  $\text{FA}_{0.83}\text{Cs}_{0.17}\text{Sn}_x\text{Pb}_{1-x}\text{I}_3$  thin films, shown for different tin fractions as labelled in each sub-figure. The  $\text{SnF}_2$  percentage added to the tin precursor solution during preparation is indicated in the legend. The spectrum for the 20%  $\text{SnF}_2$  condition at each tin fraction is subtracted as the phonon contribution, which results in a uniformly 0 spectrum for this  $\text{SnF}_2$  percentage in each panel on the right of the figure. The raw spectra for samples with  $x = 1$  in the top left sub-figure here are also shown in Figure 3A in the main text.

## 5 Photoluminescence lifetime analysis

As the example set of photoluminescence decay transients in Figure S8 shows, PL decay dynamics for  $\text{FA}_{0.83}\text{Cs}_{0.17}\text{Sn}_x\text{Pb}_{1-x}\text{I}_3$  samples vary widely across the range from lead to tin, particularly when tin fluoride is added. In addition to the large variation in lifetimes, the observed decay dynamics are closer to monoexponential in character (appearing linear on the semilog scale used in Figure S8) for high tin fractions than low tin fractions. This trend can be considered in the context of the rate equation previously used for change in the photoexcited charge carrier population over time in the presence of a background hole doping density  $p_0$ , where photoexcited electron and hole densities  $n$  and  $p$  are assumed to be equal :<sup>S31,S32</sup>

$$\frac{dn}{dt} = -(k_1^{nr} + k_2^r p_0)n - k_2^r n^2 \quad (9)$$

Here the rate constants are  $k_1^{nr}$  for nonradiative monomolecular recombination, most commonly a trap-assisted process, and  $k_2^r$  for radiative bimolecular recombination between free electrons and holes. The term  $k_2^r p_0$  can also be expressed as a radiative monomolecular rate constant  $k_1^r$  for recombination between photoexcited electrons and the background hole population. It can be seen from this equation that at low fluences and high background hole densities, the monomolecular recombination term dominates and monoexponential decay is expected with time constant  $(k_1^{nr} + k_2^r p_0)^{-1}$ . This is the scenario that applies for perovskites with high tin fraction in this study, which have high background hole doping densities above  $10^{18} \text{ cm}^{-3}$  (as shown in Figure 3B of the main text) and for which comparatively low initial photoexcited charge-carrier densities on the order of  $10^{15} - 10^{17} \text{ cm}^{-3}$  were used here. Consequently, the bimolecular recombination term in Equation 9 is negligible for perovskites with high tin fraction, whereas at higher fluences and with lower  $p_0$  the contribution of the bimolecular term becomes more significant and the decay is non-exponential. Non-exponential decay dynamics can also arise in the trap-mediated monomolecular recombination regime

at low fluence, for example when there is a spatially inhomogeneous distribution of trap states,<sup>S31,S33</sup> and have often been observed for lead-based perovskites.<sup>S34–S36</sup>

To account for the varying decay dynamics across the tin-lead range, we here fit each measured decay transient with a stretched exponential of the form given in Equation 10,

$$I(t) = A \exp \left( - \left( \frac{t}{k} \right)^\beta \right) \quad (10)$$

where the stretching parameter  $\beta$  is equal to 1 for monoexponential decay and takes smaller values with increasing stretching. Stretched exponential fits have long been used to analyse PL decay transients for lead-based perovskites,<sup>S34–S37</sup> and encompass the case of a monoexponential decay as  $\beta$  approaches 1, making the use of Equation 10 suitable for both majority lead and majority tin compositions. The effective lifetime is then given by Equation 11.

$$\tau_{eff} = \frac{k}{\beta} \Gamma \left( \frac{1}{\beta} \right) \quad (11)$$

The range to fit, as shown by the solid lines in Figure S8, extended from 0.8 ns after the peak PL intensity to 1% of the maximum intensity for each measured decay transient, in order to minimise the influence of the instrument response at early times and high noise at late times on the resulting fit. The importance of the offset of 0.8 ns from the peak used to define the range to fit can be seen from the slight positive curvature of the decay transients close to the peak, which is apparent in many cases including for the samples with short-lived PL .

Examining values of  $\tau_{eff}$  and  $\beta$  obtained from these stretched exponential fits, as shown for the full set of tin fractions and tin fluoride percentages covered in Figure S9, the experimental error indicated by the ranges of values for the six equivalent samples at  $x = 0$  is relatively large, indicating that for many tin fractions there is not a significant difference between most of the tin fluoride percentages added. Taking this into account, we can still identify several trends of interest. First, the PL lifetime generally decreases with increasing

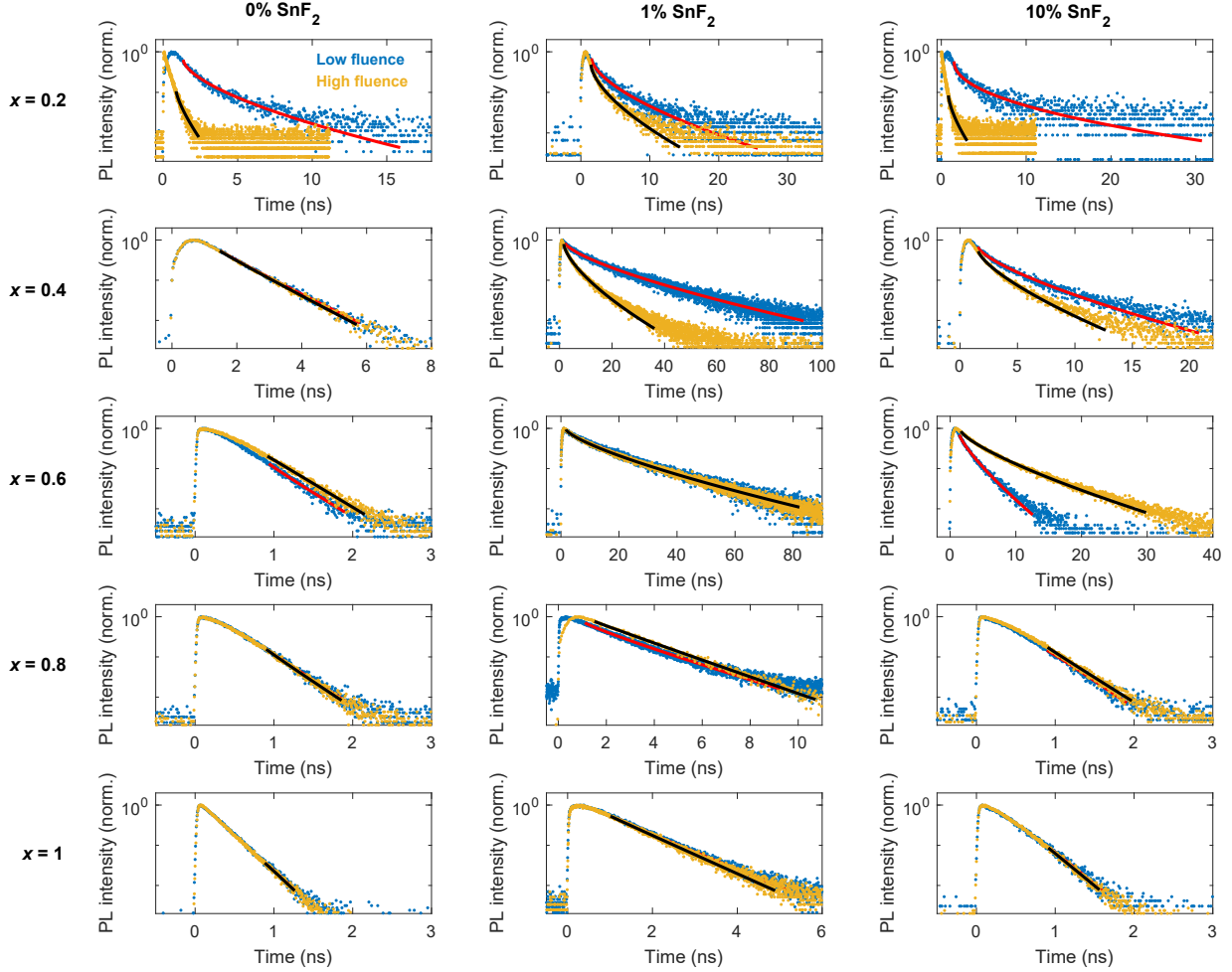


Figure S8: Example PL decay transients for  $\text{FA}_{0.83}\text{Cs}_{0.17}\text{Sn}_x\text{Pb}_{1-x}\text{I}_3$  thin films on z-cut quartz at tin fractions as indicated, with 0, 1, or 10%  $\text{SnF}_2$  added to the tin precursor solution during preparation, with stretched exponential fits used to extract effective lifetimes. Low fluence decay transients (data points in blue, fitted curves in red) were measured with excitation at  $59 \text{ nJ cm}^{-2}$ , high fluence decay transients (gold data points, fitted curves in black) were measured with excitation at  $500 \text{ nJ cm}^{-2}$ , with excitation wavelength 405 nm in both cases. For each sample, PL decay transients were measured at the peak emission energy as determined from time integrated PL spectra.

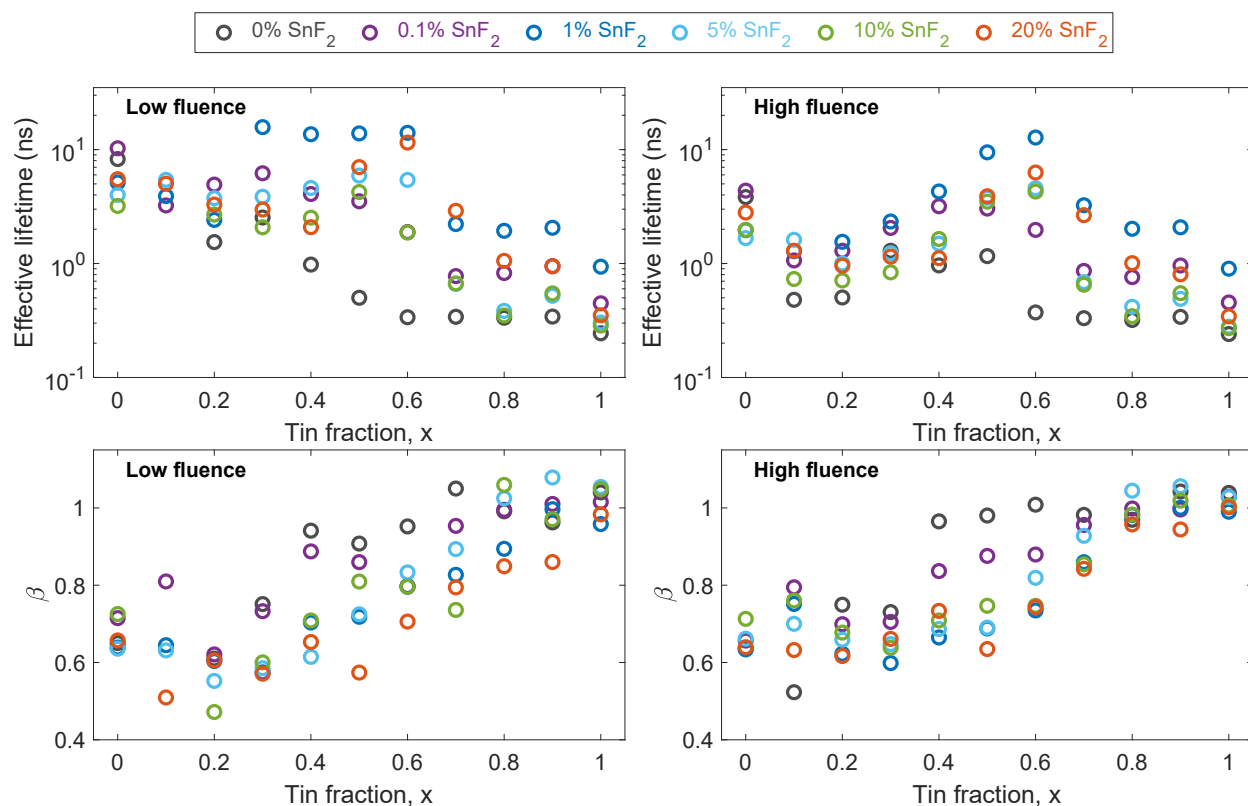


Figure S9: Effect of different amounts of SnF<sub>2</sub> additive on photoluminescence decay dynamics of FA<sub>0.83</sub>CS<sub>0.17</sub>Sn<sub>x</sub>Pb<sub>1-x</sub>I<sub>3</sub> thin films on z-cut quartz with varying tin fraction  $x$ , quantified by effective lifetime and stretching parameter  $\beta$  from stretched exponential fits. Samples were excited at 450 nm with 59 nJ cm<sup>-2</sup> for the low fluence condition, 500 nJ cm<sup>-2</sup> for the high fluence condition. Note that SnF<sub>2</sub> was added to the tin precursor during preparation, so the spread of values for samples with  $x = 0$  reflects experimental error and variation between sets of samples without any change in composition.

tin fraction, and is enhanced by the addition of tin fluoride with particularly large effect for tin fractions 0.5 and 0.6. Adding 1% tin fluoride appears to give the largest improvements in PL lifetime across the range. Figure 3C of the main text shows the mean effective lifetime for the tin fractions at which we were able to calculate hole doping densities, and illustrates this trend more simply, with all  $\text{SnF}_2$  percentages giving an increase in lifetime compared to the samples without any tin fluoride added, and similar lifetimes for 0.1, 5, and 10%  $\text{SnF}_2$  addition while 1% gives even longer lifetime.

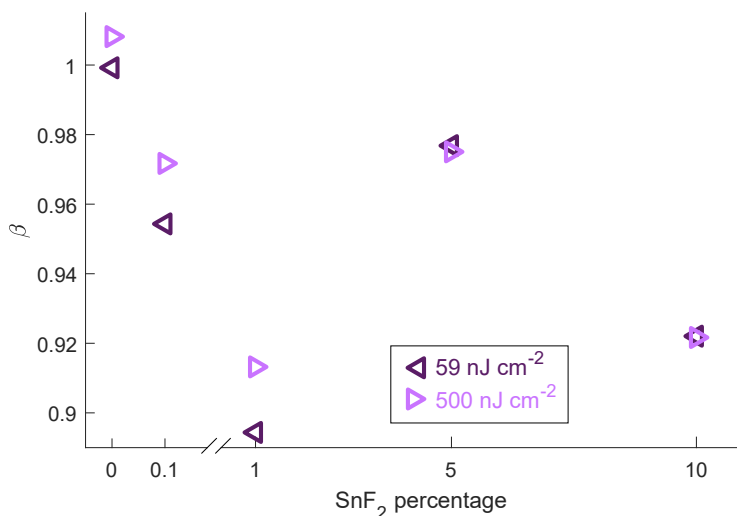


Figure S10: Effect of different amounts of  $\text{SnF}_2$  additive on the stretching parameter,  $\beta$ , fitted to measured PL decay transients of  $\text{FA}_{0.83}\text{Cs}_{0.17}\text{Sn}_x\text{Pb}_{1-x}\text{I}_3$  thin films, where values closer to 1 correspond to a decay profile closer to monoexponential. Values shown are the mean for compositions within fraction 0.6 – 1, corresponding to the lifetimes shown in Figure 3C of the main text, with the same marker colour scheme also used.

Considering the stretching parameter, the underlying trend is of a shift from more stretched decay transients at low tin fractions, which would be expected in either a trap-mediated or bimolecular recombination regime as discussed above, to monoexponential decay at high tin fractions. The addition of tin fluoride leads to generally smaller  $\beta$  values particularly for the intermediate tin fractions 0.4 to 0.7, and there is less effect from addition of 0.1%  $\text{SnF}_2$  than for larger percentages, with the greatest reductions in  $\beta$  generally apparent for 1% or 20% tin fluoride addition. Figure S10 shows the mean stretching parameter values

over the set of samples for which background hole densities were calculated, as in Figure 3C of the main text. Comparing these averaged values, the reduction in  $\beta$  with tin fluoride addition to suppress background hole doping remains apparent. The decrease in  $\beta$  with tin fluoride addition and with decreasing tin fraction reflects the drop in background hole doping density, which reduces the contribution of the  $k_2^r p_0$  decay term in Equation 9 as a smaller proportion of photoexcited charge carriers recombine with background holes and the underlying non-exponential decay dynamics become more prominent.

## 6 Analysis of absorbance spectra

Comparing the absorbance spectra measured for  $\text{FA}_{0.83}\text{Cs}_{0.17}\text{Sn}_x\text{Pb}_{1-x}\text{I}_3$  samples across the range from lead to tin with varying tin fluoride percentage, shown in Figure S11, several differences in the spectra with changing sample composition are apparent. As tin fraction  $x$  increases, the absorption onset can be seen first to shift to longer wavelength (and correspondingly lower energy) and then back to shorter wavelength for  $x = 1$  than for several of the intermediate compositions. With varying amounts of  $\text{SnF}_2$  added, denoted by different line colours as indicated in the legend, there is little change in absorption onset for samples with low tin fraction, but some variation in scattering between samples which affects the baseline absorbance value below bandgap and offsets spectra vertically. For higher tin fractions, and most obviously at  $x = 1$ , it also appears that there is a shift in the absorption onset with tin fluoride addition, moving from higher to lower energy when 1% tin fluoride or greater is used. To quantify these shifts, and see the resulting trends clearly, we determine the optical bandgap from each measured spectrum, and analyse fits for the bandgap bowing parameter, as described below.

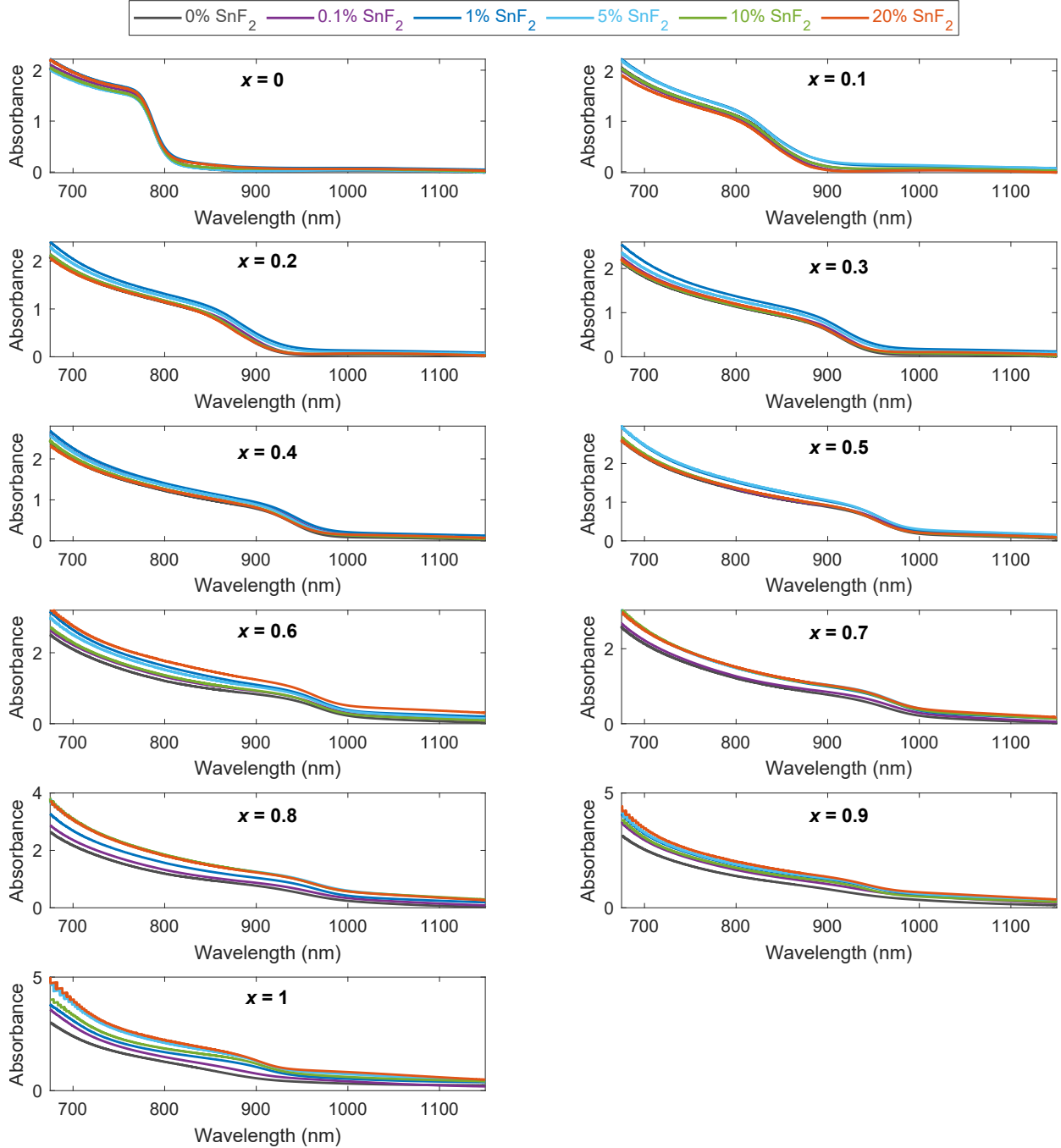


Figure S11: Absorbance spectra of  $\text{FA}_{0.83}\text{Cs}_{0.17}\text{Sn}_x\text{Pb}_{1-x}\text{I}_3$  thin films on z-cut quartz with tin fractions as indicated across the range from neat tin to neat lead, and different amounts of tin fluoride added to the tin precursor solution during preparation as indicated in the legend. Absorbance,  $A$ , is calculated from measured reflectance and transmittance spectra according to  $A = -\ln(T/(1-R))$ . Note that the tin fluoride percentages shown in the legend correspond to  $\text{SnF}_2$  added to the tin precursor solution, and so in the case of  $x = 0$  the six spectra plotted were measured on individual samples prepared as part of the set with the corresponding percentage of  $\text{SnF}_2$  added, but without changing the composition at  $x = 0$  between sets, as the actual  $\text{SnF}_2$  content at  $x = 0$  is 0% in all cases.

## 6.1 Determining bandgap

As a measure of the optical bandgap determined from absorbance spectra we use the absorption edge, defined as the point with the steepest gradient in the onset region of the absorbance spectrum. This method has previously been identified to yield more physically sensible results than the use of a Tauc plot<sup>S38</sup> which ignores the influence of excitons, while being suitable for use in cases where fits using the full formula from Elliott theory<sup>S39</sup> are made impractical by the scatter and reflection from the samples.<sup>S31</sup> Figure S12 illustrates the process of applying the steepest gradient method for a representative example spectrum at tin fraction 0.6, showing the existence of a clear maximum in the gradient (panel B) over the onset region, and illustrating the position of this steepest point on the spectrum in panel A.

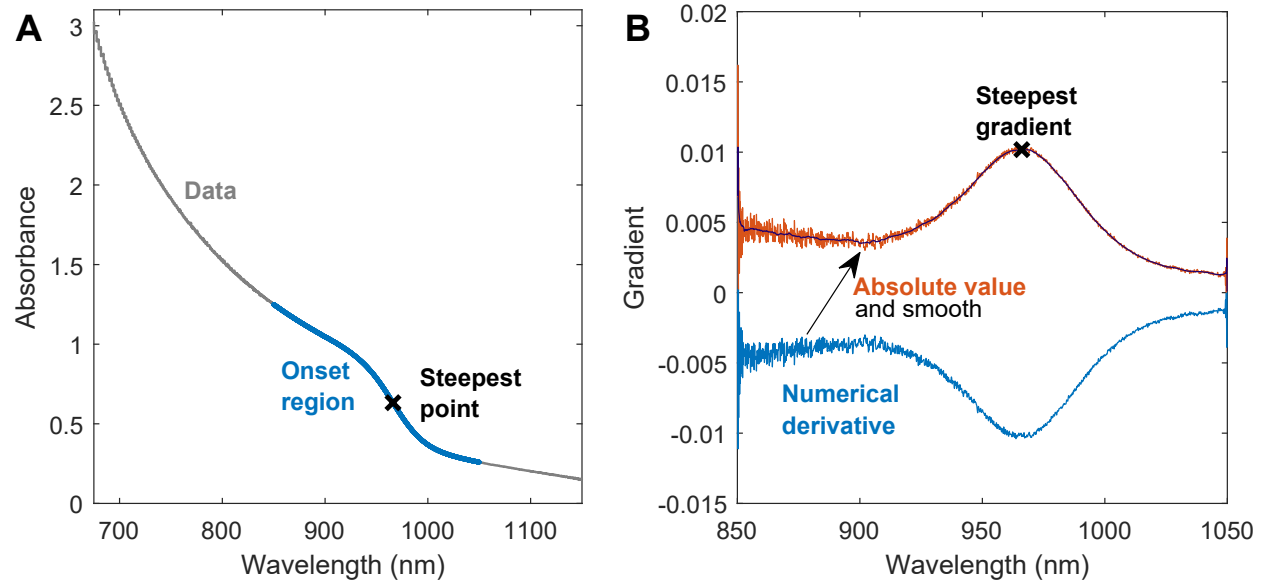


Figure S12: Illustration of the steepest gradient method used to determine  $E_g$  from measured absorbance spectra. (A) Absorbance spectrum of  $\text{FA}_{0.83}\text{Cs}_{0.17}\text{Sn}_{0.6}\text{Pb}_{0.4}\text{I}_3$  thin film on z-cut quartz substrate, prepared with 5%  $\text{SnF}_2$  added, showing the identified steepest gradient point and the onset region differentiated to identify this point, as shown in panel B. (B) Gradient of the onset region identified in panel A determined by numerical differentiation, showing the maximum point identified after smoothing.

The absorption edge values determined in this way for the full set of compositions across the range from lead to tin, illustrating the effect of tin fluoride percentage, are shown in

Figure S13 below as well as in Figure 4A of the main text, where both the bandgap bowing and the reduction in bandgap with tin fluoride addition observed qualitatively from spectra in Figure S11 can be seen clearly. The bandgap bowing trends seen are further explored with fits to extract bowing parameters as shown in Figure S13 below.

## 6.2 Bandgap bowing fits

The phenomenon of bandgap bowing seen in the absorption onsets for  $\text{FA}_{0.83}\text{Cs}_{0.17}\text{Sn}_x\text{Pb}_{1-x}\text{I}_3$  thin films with varying tin fraction where the change in bandgap is not linear with composition is known for alloys of many inorganic semiconductors<sup>S40,S41</sup> as well as in perovskites.<sup>S9,S42</sup> Variations in average crystal potential and aperiodic disorder effects have both been identified to contribute to bandgap bowing for inorganic semiconductor alloys<sup>S43,S44</sup> with later works concluding that structural relaxation through bond stretching plays a significant role, along with redistribution of charge and volume deformation relative to the neat compositions.<sup>S45-S47</sup> In tin-lead perovskites, recent works have identified bond bending<sup>S31</sup> as the main contributor to bandgap bowing, with the chemical effects from orbital energy mismatch between the two metals playing a smaller role.<sup>S42</sup> For both hybrid metal halide perovskites and inorganic semiconductors the trend in bandgap energies can be described by Equation 12<sup>S41,S43,S48</sup> where  $E_i$  are the bandgaps of the two neat compositions, mixed in a ratio  $x$ , and  $b$  is the bowing parameter describing the deviation from linearity.

$$E(x) = E_1x + E_2(1 - x) - bx(1 - x) \quad (12)$$

Figure S13 shows the results of fitting Equation 12 to the optical bandgap values determined as described in Section 6.1 for  $\text{FA}_{0.83}\text{Cs}_{0.17}\text{Sn}_x\text{Pb}_{1-x}\text{I}_3$  samples with varying amounts of tin fluoride added to the tin precursor solution during preparation. The fitted curves (solid lines) follow the data closely for tin fluoride percentages of 1% and above, but there is a clear deviation from the data at tin fractions close to 1 for 0.1%  $\text{SnF}_2$ , and for 0% there is

also deviation for low tin fractions, showing a poor fit overall. The fitted bowing parameter,  $b$ , is larger for these two cases where the fit is poor, whereas for 1-20% SnF<sub>2</sub> similar values of  $b$  are obtained in each case.

Comparing the bowing parameter values fitted here with previous reports, the values of 0.69 – 0.73 eV for FA<sub>0.83</sub>Cs<sub>0.17</sub>Sn <sub>$x$</sub> Pb<sub>1- $x$</sub> I<sub>3</sub> with 1% SnF<sub>2</sub> or greater are similar to those previously found for similar perovskites FA<sub>0.8</sub>Cs<sub>0.2</sub>Sn <sub>$x$</sub> Pb<sub>1- $x$</sub> I<sub>3</sub>, with  $b = 0.75$  eV,<sup>S42</sup> and FASn <sub>$x$</sub> Pb<sub>1- $x$</sub> I<sub>3</sub>, with  $b = 0.73$  eV.<sup>S31</sup> This agreement further highlights the deviation in fitted  $b$  values for samples with 0% and 0.1% SnF<sub>2</sub> added during preparation, where the variation in bandgap is not well accounted for by this bowing model. As can be seen in Figure S13, and more clearly in Figure 4A where the data for each tin fluoride percentage are overlaid, the increase in bandgap with less than 1% SnF<sub>2</sub> that leads to larger fitted  $b$  values and a worse fit to the data only affects samples at high tin fractions.

These high tin fraction samples also show much higher background hole doping densities for 0 and 0.1% SnF<sub>2</sub>, as shown in Figure 3B of the main text. The increase in bandgap distorting the expected bandgap bowing trend can therefore be attributed to the Burstein-Moss effect<sup>S49,S50</sup> where as a result of significant hole doping the highest occupied states in the valence band from which electrons can be photoexcited are found below the valence band maximum, leading to a blueshift in absorption relative to the undoped case. This effect has previously been observed in MASnI<sub>3</sub> and FASnI<sub>3</sub>, which show large blueshifts in the absorption onset that can be suppressed by the addition of between 5 and 20% SnF<sub>2</sub>.<sup>S25,S51</sup> The blueshift in the bandgap that we observe for neat tin samples ( $x = 1$ ) here is consistent with previous reports, and we find that a Burstein-Moss shift can also be seen for mixed tin-lead perovskites with high tin content, most clearly for tin fraction 0.9.

$$E(x) = E_{\text{Sn}}x + E_{\text{Pb}}(1-x) - bx(1-x)$$

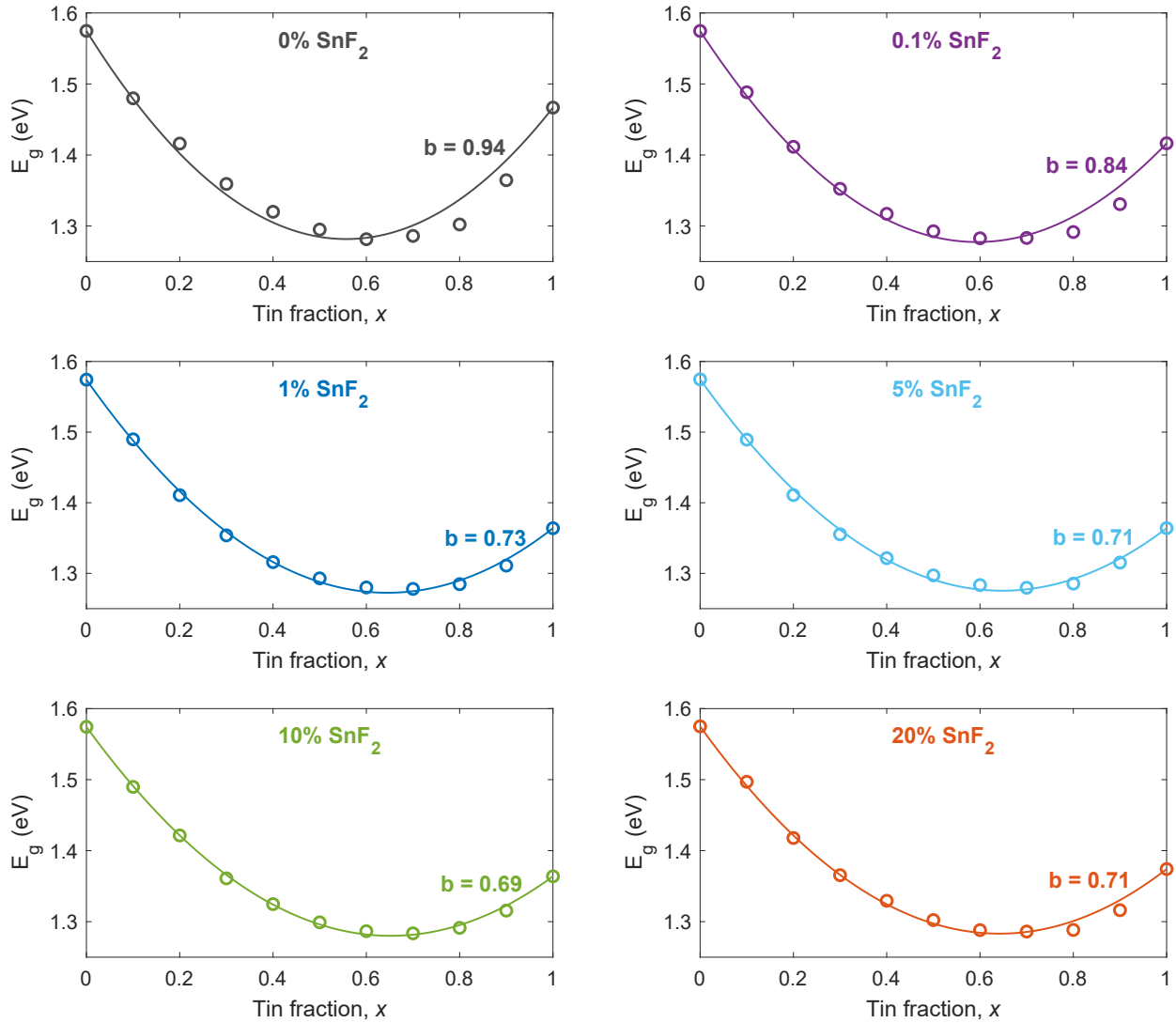


Figure S13: Optical bandgap of  $\text{FA}_{0.83}\text{Cs}_{0.17}\text{Sn}_x\text{Pb}_{1-x}\text{I}_3$  samples across the range from lead to tin with between 0 and 20%  $\text{SnF}_2$  added during preparation, and fits using the equation shown for bandgap bowing, showing deviation from the model for 0 or 0.1%  $\text{SnF}_2$ . Bandgap values (open circle markers) are as shown in Figure 4A, determined from the absorbance spectra of thin films by the steepest gradient method, and fits are shown as solid lines, with bowing parameter values as indicated.

## 7 Analysis of photoluminescence spectra

### 7.1 Details of spectral response correction

As illustrated in Figure S13 above, and Figure 4A of the main text,  $\text{FA}_{0.8}\text{Cs}_{0.2}\text{Sn}_x\text{Pb}_{1-x}\text{I}_3$  samples across the compositional range from  $x = 0$  to  $x = 1$  have optical bandgaps covering an energy range of several hundred meV into the near infrared. The emission spectra of these samples therefore span a similar energy range, such that neither a visible nor an infrared detector is ideally suited for measurements on all compositions. We therefore use both a silicon CCD (with strong response through the visible range) and an InGaAs array (best suited to measurements in the near infrared range) to measure PL spectra, as described in Section 4 of the main text.

Each measured spectrum was individually corrected for the spectral response of the relevant detector, determined by comparison of the measured and known reference spectrum for a tungsten filament lamp (OL245 U). After applying this spectral response correction, the spectra for a given sample measured on each of the two detectors agreed closely as can be seen from the spectra plotted in light blue and orange in Figure S14, but some artefacts and increases in noise remained for the spectral regions where detector response dies off in each case. These undesirable features are evident in Figure S14, where the spectrum measured on the silicon detector for the sample with  $x = 0.6$  shows an artificial dip in intensity around 1030 nm and increasing noise to longer wavelengths, while the spectra measured on the InGaAs detector for samples with  $x = 1$  and  $x = 0$  show a similar small dip around 890 nm and a larger artificial step at 745 nm related to the onset of detection.

In order to eliminate these artefacts and give a single spectrum for each sample to be used in subsequent analysis of broadening and peak position, we combine the data from both detectors according to Equation 13.

$$I(E) = \left( \frac{W_{\text{Si}}(E)}{W_{\text{Si}}(E) + W_{\text{IGA}}(E)} \right) I_{\text{Si}}(E) + \left( \frac{W_{\text{IGA}}(E)}{W_{\text{Si}}(E) + W_{\text{IGA}}(E)} \right) I_{\text{IGA}}(E) \quad (13)$$

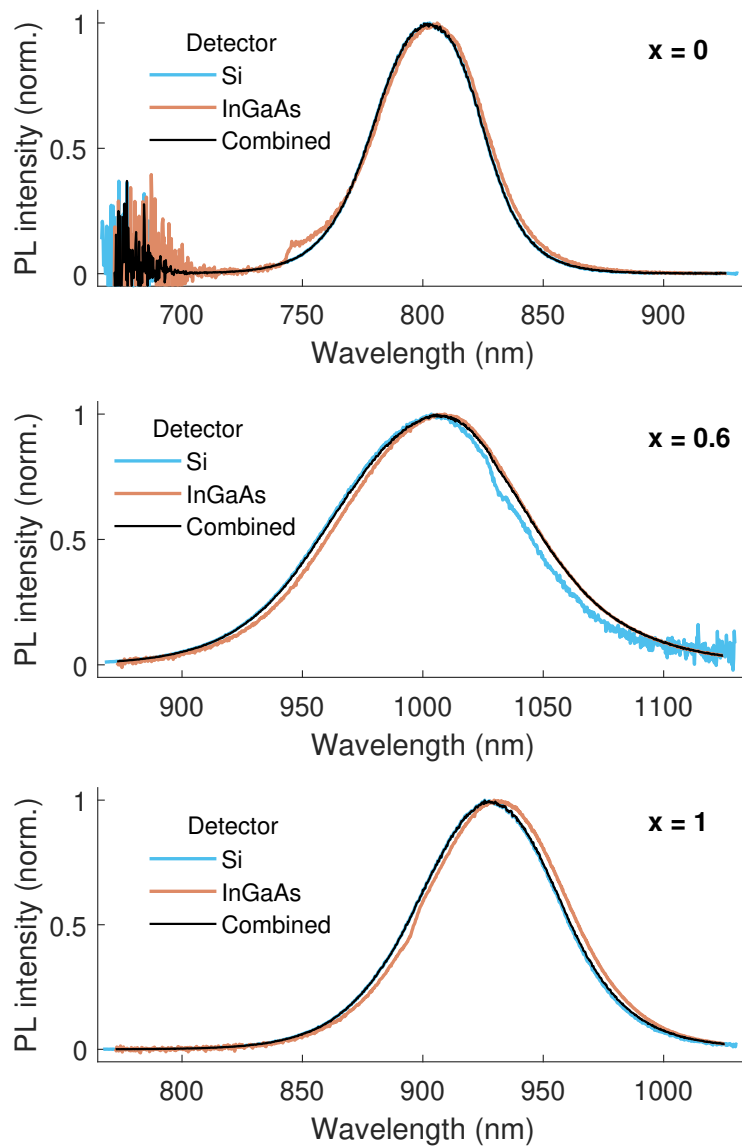


Figure S14: Example photoluminescence spectra before and after combining data from the two detectors for  $\text{FA}_{0.83}\text{Cs}_{0.17}\text{Sn}_x\text{Pb}_{1-x}\text{I}_3$  thin films with 1%  $\text{SnF}_2$  added during preparation and tin fraction  $x$  as indicated. Each panel shows the spectra measured on the Si CCD (light blue) and InGaAs array (orange) detectors after applying a spectral response correction, as well as the combined spectrum (black) according to Equation 13 which gives greater weight to the detector with the stronger response at each point in the spectrum, and eliminates the artefacts seen in regions of low detector response. The samples for which PL spectra are shown here have emission spanning the full range observed for varying tin fraction  $x$ .

The normalised intensity data from measurements on Si and InGaAs detectors (light blue and orange respectively in Figure S14) enter as  $I_{\text{Si}}$  and  $I_{\text{IGA}}$  and the contribution from each detector in the final spectrum (plotted in black in Figure S14) is based on the ratio of the weighting functions  $W_{\text{Si}}$  and  $W_{\text{IGA}}$  which model the drop off in/onset of detector sensitivity as smoothly varying error functions as shown in Figure S15. The specific forms of  $W_{\text{Si}}$  and  $W_{\text{IGA}}$  as shown were chosen to preserve the crossover in intensity between the two detectors observed experimentally to occur at 1006 nm for our setup.

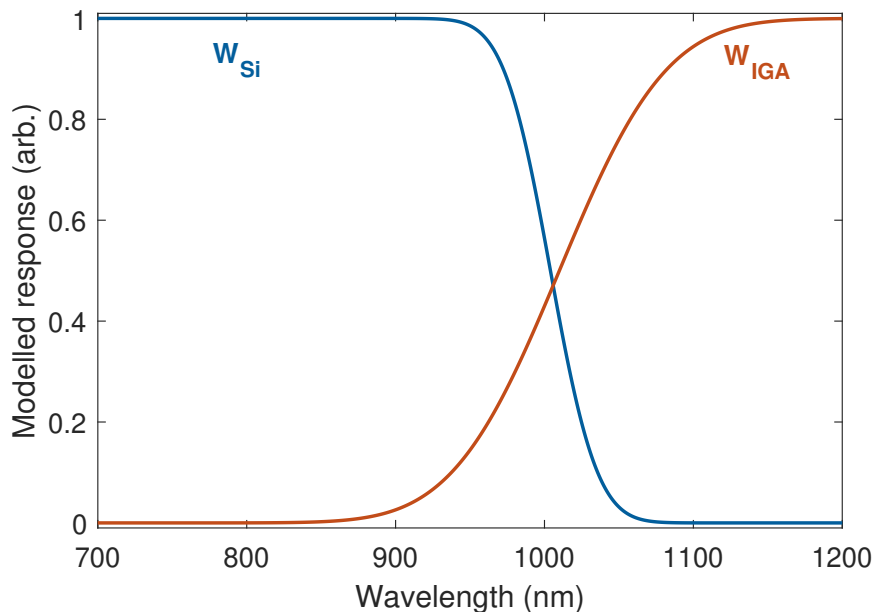


Figure S15: Weighting functions used in Equation 13 to combine data from the Si CCD and InGaAs array detectors into a single spectrum. These functions model the drop off/rise in sensitivity for each detector over the wavelength range of interest using the error function, with the crossover point between the two curves matching the experimentally observed crossover wavelength of 1006 nm.

The use of Equation 13 thus allows data from the two detectors to be smoothly combined for each sample in a consistent fashion taking into account the spectral variations in detector responsivity, rather than making a choice of which spectrum to use for a given sample based on whether the measured peak falls above or below a nominated energy cutoff. This is particularly beneficial given that most spectra are significantly broadened and so the full spectrum for a single sample is often not well captured by either detector alone. The shape

and peak position of the final spectra, as shown in black in Figure S14, closely reflect the original data with artefacts from low detector response now eliminated. Further examples of photoluminescence spectra combining data from both detectors, as used in subsequent analysis, are shown in Figure S16.

## 7.2 Trends in PL peak position

The photoluminescence spectra of  $\text{FA}_{0.83}\text{Cs}_{0.17}\text{Sn}_x\text{Pb}_{1-x}\text{I}_3$  samples with varying tin fraction are expected to reflect the bandgap bowing discussed in Section 6.2 and illustrated in Figure 4A of the main text, and as the sets of spectra shown in Figure S16 illustrate there is indeed a shift to emission at lower energies as  $x$  increases from 0 to 0.6 or 0.7 followed by a smaller blueshift relative to the lowest energy emission for the higher tin compositions. However, there is a noticeable lack of PL peaks intermediate in energy between the neat lead ( $x = 0$ ) and neat tin ( $x = 1$ ) compositions, in contrast to the trend in optical bandgaps determined from absorption onset. Comparing the three panels in Figure S16 the emission spectra at each tin fraction appear similar for 0, 1, and 20%  $\text{SnF}_2$ , with no apparent changes in peak position even for high tin compositions where the absorption onset does shift with  $\text{SnF}_2$  percentage due to the Burstein-Moss effect.

Figure S17 shows the energy of the  $\text{FA}_{0.83}\text{Cs}_{0.17}\text{Sn}_x\text{Pb}_{1-x}\text{I}_3$  PL peak against tin fraction  $x$  for all six tin fluoride percentages, allowing the trends identified above from Figure S16 to be seen more clearly. Comparing the peak energies for different tin fluoride percentages there is no clear trend across all tin fractions, and in many cases the spread in values is comparable to that seen for the samples at  $x = 0$  which were all prepared with 0%  $\text{SnF}_2$  (as noted in Section 1.1 above) and are colour coded in Figure S17 and Figure 4 in the main text according to the set with which each sample was made. Since each of these  $x = 0$  samples was prepared to the same recipe, the range of peak positions seen for this composition gives an indication of sample to sample variation and measurement error, indicating that for most tin fractions there is no significant difference in PL peak energy with tin fluoride addition.

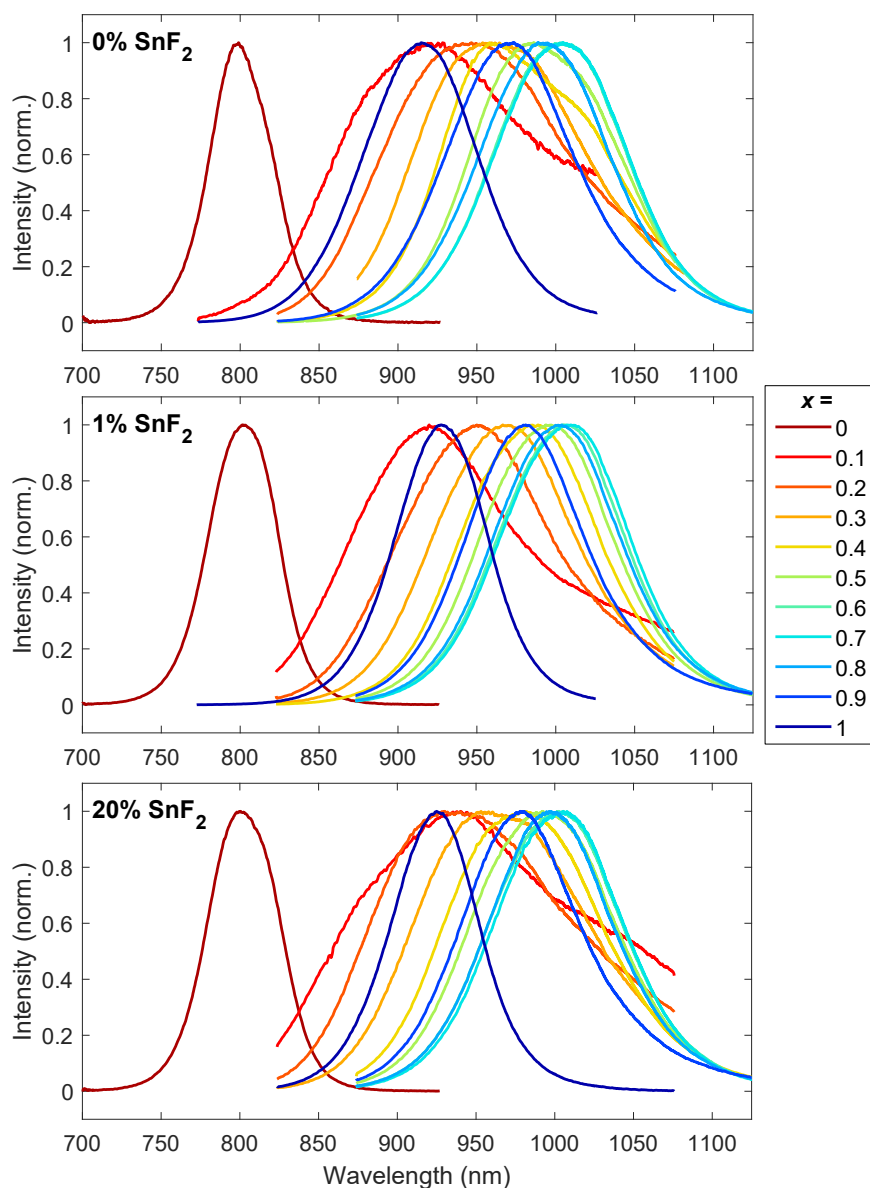


Figure S16: Representative sets of photoluminescence spectra of  $\text{FA}_{0.83}\text{Cs}_{0.17}\text{Sn}_x\text{Pb}_{1-x}\text{I}_3$  thin films on z-cut quartz, with 0, 1 or 20%  $\text{SnF}_2$  added during preparation as indicated. Samples were excited with a CW laser at 532 nm,  $1.8 \text{ W cm}^{-2}$ , and measurements taken using both Si and InGaAs detectors before correcting and combining the spectra from both detectors as illustrated in Figure S14 and smoothing to give the spectra shown here. The same colour scheme for tin fraction  $x$  is used in all three panels, indicated in the legend.

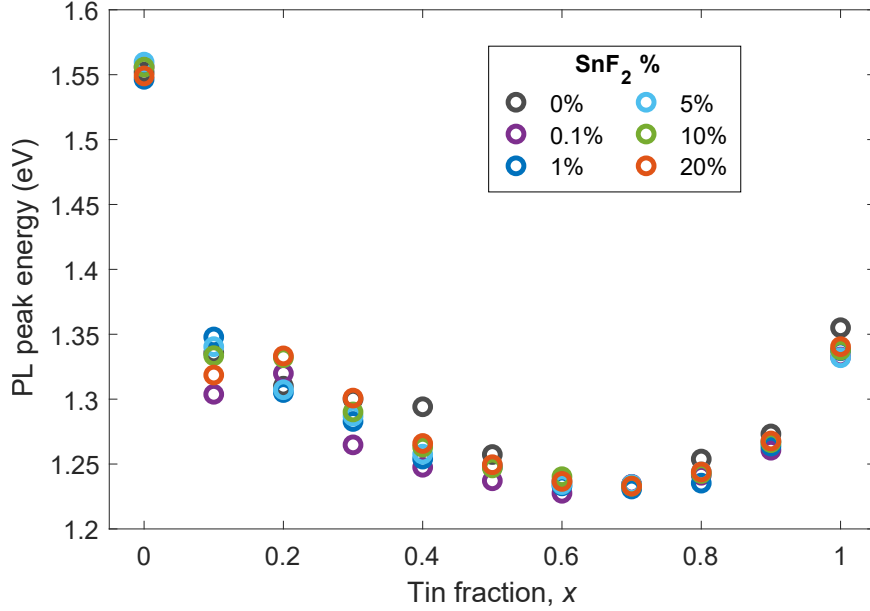


Figure S17: Energy of the photoluminescence peak for  $\text{FA}_{0.83}\text{Cs}_{0.17}\text{Sn}_x\text{Pb}_{1-x}\text{I}_3$  thin films on z-cut quartz across the range from neat lead to neat tin with different amounts of tin fluoride added to the tin precursor solution during preparation, as indicated in the legend. Photoluminescence spectra were measured with  $1.8 \text{ W cm}^{-2}$  excitation from a 532 nm CW laser. The colour scheme used for tin fluoride percentage is the same as in Figure 4C of the main text, where the Stokes shifts shown were calculated from these peak positions and the absorption edge  $E_g$  value. The large redshift in emission energy for low tin fractions due to the presence of defects, deviating from the expected trend in bandgap, can be clearly seen here.

The effect of tin fraction on PL peak energy is clearer, and can be explained by two key factors. First, the underlying trend of bandgap bowing for mixed tin-lead perovskites described in Section 6.2 and seen for samples prepared with 1%  $\text{SnF}_2$  or greater in Figure S13 and Figure 4A of the main text is reflected in the PL peak energies seen here for  $x = 0.5 - 1$  for all tin fluoride percentages. There is no Burstein-Moss shift seen here, since photoexcited electrons from absorption above the bandgap in the case of high hole doping concentrations still relax down to the band edge and recombine radiatively with the same energy as if the initial excitation had occurred from states higher in the valence band.

For the low tin fractions,  $x = 0.1 - 0.4$ , the trend in peak energy does not closely follow that seen in the absorption edge due to bandgap bowing but instead shows a large redshift in emission energy immediately for the change from neat lead to tin fraction 0.1,

with smaller redshifts as tin content increases thereafter. This leads to the large Stokes shifts seen in Figure 4C of the main text for low tin fractions. We attribute the large drop in emission energy for low tin fractions to defects present in these films, which also exhibit significant energetic disorder leading to broadening of PL spectra as seen for the example sets of spectra plotted in Figure S16 and quantified as FWHM in Figure 4B of the main text. As a similarly large redshift in PL peak energy at low tin fractions is observed with or without tin fluoride, and there is not a clear trend with varying amounts of tin fluoride, we conclude that incorporation of small amounts of tin introduces defects giving low-energy states from which recombination can occur, regardless of the background hole doping density from oxidation of tin. Similar PL redshifts at low tin fraction have been reported previously for  $\text{FASn}_x\text{Pb}_{1-x}\text{I}_3$ ,<sup>S31</sup>  $\text{MASn}_x\text{Pb}_{1-x}\text{I}_3$ ,<sup>S14</sup> and  $\text{CsSn}_x\text{Pb}_{1-x}\text{I}_3$ <sup>S52</sup> which supports this conclusion.

High defect densities at low tin fractions, and a corresponding increase in sub-bandgap states, are also indicated by large Urbach energies calculated previously.<sup>S11,S53</sup> Considering the origin of these sub-bandgap defect states, we note that the XRD patterns we measure for low tin fraction samples, like those for the rest of the compositional range, do not show impurity peaks from precursors or non-perovskite phases (see Section 2.1 for a full discussion of this.) Additionally, the perovskite XRD peaks do not show significant broadening for tin fractions 0.1 – 0.4 compared to the rest of the compositional range, as shown by the FWHM values in Figure 1B of the main text. We therefore consider it unlikely that phase changes or large scale structural disorder contribute to the observed defectiveness at low tin fractions, with changes in the energy of trap states being a more likely explanation.

## 8 Calculating charge-carrier mobility from OPTP measurements

The sum mobility of the photoexcited charge carriers,  $\mu$ , was estimated from the onset of the THz photoconductivity (shown in Figure S18) at time = 0, using the Drude model of low-frequency (DC) conductivity:<sup>S54</sup>

$$\sigma_{\text{photo}}(t) = [\mu_e n(t) + \mu_h p(t)] e \stackrel{t=0}{=} \mu n_0 e \quad (14)$$

where  $\mu_e$  and  $\mu_h$  are the individual mobilities of electrons and holes,  $\mu$  is the sum mobility of the charge carriers ( $\mu_e + \mu_h = \mu$ ),  $n$  and  $p$  are the number densities of photoexcited electrons and holes respectively,  $n_0$  is the initial number density of the photoexcited electron-hole pairs, and  $e$  is the elementary charge.

Table S5: Photoexcitation beam fluences used for terahertz photoconductivity decay measurements as shown in Figure S18.

Fluence set ( $\mu\text{J cm}^{-2}$ )			Samples measured
Low	Medium	High	
1.33	7.53	12.74	$x = 0.7$ : 0, 0.1, 1, and 20% SnF <sub>2</sub>
1.47	8.13	13.97	$x = 0.6$ : 0, 1, 10 and 20% SnF <sub>2</sub> . $x = 1$ : 0, 1, 10 and 20% SnF <sub>2</sub>
1.97	10.77	18.1	$x = 0.6$ : 0.1% SnF <sub>2</sub> $x = 0.8$ : 0, 0.1, 1, and 20% SnF <sub>2</sub> $x = 0.9$ : 0, 0.1, 1, and 20% SnF <sub>2</sub> $x = 1$ : 0.1% SnF <sub>2</sub>
2.36	13.26	22.5	$x = 0.7$ : 10% SnF <sub>2</sub> . $x = 0.8$ : 10% SnF <sub>2</sub> $x = 0.9$ : 10% SnF <sub>2</sub> .

The initial density of photoexcited charge carrier pairs,  $n_0$ , was calculated using steady-state absorption data at the pump wavelength (400 nm) and the measurements of excitation fluence (shown in Table S5), assuming that each absorbed photon resulted in a photoexcitation of one electron-hole pair (which is a good assumption because of the low exciton binding energy reported for metal halide perovskites).<sup>S23,S55-S57</sup> The mobilities stated in the

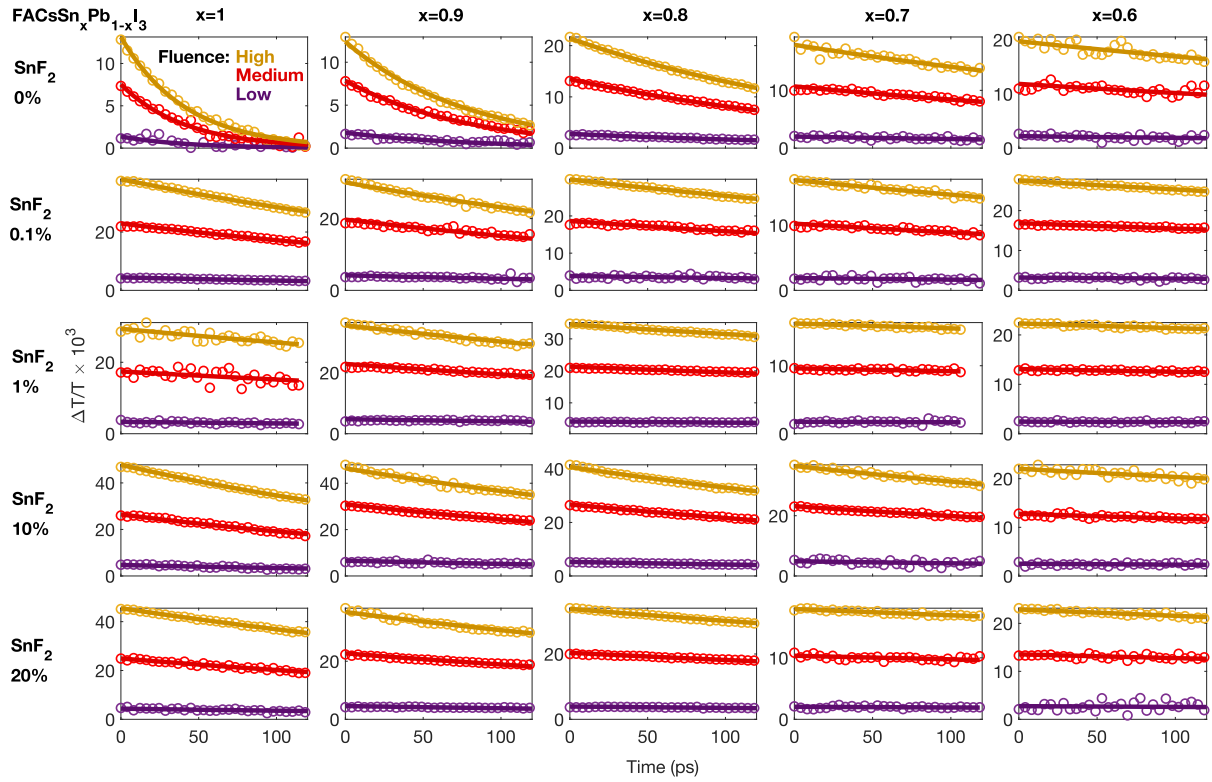


Figure S18: Photoconductivity dynamics of  $\text{FA}_{0.83}\text{Cs}_{0.17}\text{Sn}_x\text{Pb}_{1-x}\text{I}_3$  thin films shown for various tin fractions and  $\text{SnF}_2$  percentages. The photoconductivity of each sample was measured for three different excitation fluences, listed in Table S5.

main text (Figure 5) were calculated for each thin film included in Figure S18 for all three excitation fluences and then averaged to obtain a single value of charge-carrier sum mobility for the sample. We note that the calculated charge-carrier mobility does not depend on the estimated thickness of the thin films (described in Section 3.1) as the thickness dependence of the calculated photoconductivity (Equation 4) and of the initial density of photoexcited charge carrier pairs cancel out.<sup>S23</sup>

## 9 Fitting empirical relationship between mobility and doping density

As described in Section 2.5 of the main text, we carried out fits to calculated charge-carrier mobilities using the empirical relationship between mobility and doping density in equation 15 given by Hilsum:<sup>S58</sup>

$$\mu = \frac{\mu_L}{1 + \sqrt{N/N_0}} \quad (15)$$

Fitted curves are plotted in Figure 5 in the main text, and the values of the lattice-scattering-limited charge-carrier mobility  $\mu_L$  and the normalising density of dopants  $N_0$  from these fits are recorded in Table S6.

Table S6: Values of the parameters in Equation 15 from the fits as shown in Figure 5 in the main text. Note that the normalising density  $N_0$  was globally optimised for all tin fractions represented here.

Tin fraction, $x$	$\mu_L$ (cm <sup>2</sup> /Vs)	$N_0$ (cm <sup>-3</sup> )
0.6	48.00	$3.76 \times 10^{19}$
0.7	55.75	$3.76 \times 10^{19}$
0.8	68.68	$3.76 \times 10^{19}$
0.9	76.26	$3.76 \times 10^{19}$
1	101.43	$3.76 \times 10^{19}$

## References

- (S1) Leijtens, T.; Prasanna, R.; Gold-Parker, A.; Toney, M. F.; McGehee, M. D. Mechanism of Tin Oxidation and Stabilization by Lead Substitution in Tin Halide Perovskites. *ACS Energy Lett.* **2017**, *2*, 2159–2165.
- (S2) Petrov, A. A.; Goodilin, E. A.; Tarasov, A. B.; Lazarenko, V. A.; Dorovatovskii, P. V.; Khrustalev, V. N. Formamidinium Iodide: Crystal Structure and Phase Transitions. *Acta Crystallogr., Sect. E: Crystallogr. Commun.* **2017**, *73*, 569–572.
- (S3) Aleksandrov, I.; Goncharov, A.; Makarenko, I.; Stishov, S. X-ray-Diffraction Study of the Equation of State and the Phase Transition in Cesium Iodide at Nearly Hydrostatic Pressure. *Phys. Rev. B* **1991**, *43*, 6194.
- (S4) Palosz, B. The Structure of  $\text{PbI}_2$  Polytypes 2H and 4H: a Study of the 2H-4H Transition. *J. Phys.: Condens. Matter* **1990**, *2*, 5285.
- (S5) Howie, R.; Moser, W.; Trevena, I. The Crystal Structure of Tin (II) Iodide. *Acta Crystallogr., Sect. B: Struct. Crystallogr. Cryst. Chem.* **1972**, *28*, 2965–2971.
- (S6) Denes, G.; Pannetier, J.; Lucas, J.; Le Marouille, J. About  $\text{SnF}_2$  Stannous Fluoride. I. Crystallochemistry of  $\alpha\text{-SnF}_2$ . *J. Solid State Chem.* **1979**, *30*, 335–343.
- (S7) Reuter, H.; Pawlak, R. Zinnhalogenverbindungen. II. Die Molekül und Kristallstrukturen von Zinn (IV)-Bromid und Iodid. *Z. Kristallogr. Cryst. Mater.* **2001**, *216*, 34–38.
- (S8) Yamanaka, T.; Kurashima, R.; Mimaki, J. X-ray Diffraction Study of Bond Character of Rutile-Type  $\text{SiO}_2$ ,  $\text{GeO}_2$  and  $\text{SnO}_2$ . *Z. Kristallogr. Cryst. Mater.* **2000**, *215*, 424–428.
- (S9) Hao, F.; Stoumpos, C. C.; Chang, R. P. H.; Kanatzidis, M. G. Anomalous Band Gap Behavior in Mixed Sn and Pb Perovskites Enables Broadening of Absorption Spectrum in Solar Cells. *J. Am. Chem. Soc.* **2014**, *136*, 8094–8099.
- (S10) Liu, C.; Fan, J.; Li, H.; Zhang, C.; Mai, Y. Highly Efficient Perovskite Solar Cells with Substantial Reduction of Lead Content. *Sci. Rep.* **2016**, *6*, 35705.

- (S11) Zhao, B.; Abdi-Jalebi, M.; Tabachnyk, M.; Glass, H.; Kamboj, V. S.; Nie, W.; Pearson, A. J.; Puttison, Y.; Gödel, K. C.; Beere, H. E.; Ritchie, D. A.; Mohite, A. D.; Dutton, S. E.; Friend, R. H.; Sadhanala, A. High Open-Circuit Voltages in Tin-Rich Low-Bandgap Perovskite-Based Planar Heterojunction Photovoltaics. *Adv. Mater.* **2017**, *29*, 1604744.
- (S12) Prasanna, R.; Gold-Parker, A.; Leijtens, T.; Conings, B.; Babayigit, A.; Boyen, H.-G.; Toney, M. F.; McGehee, M. D. Band Gap Tuning Via Lattice Contraction and Octahedral Tilting in Perovskite Materials for Photovoltaics. *J. Am. Chem. Soc.* **2017**, *139*, 11117–11124.
- (S13) Jacobsson, T. J.; Schwan, L. J.; Ottosson, M.; Hagfeldt, A.; Edvinsson, T. Determination of Thermal Expansion Coefficients and Locating the Temperature-Induced Phase Transition in Methylammonium Lead Perovskites Using X-ray Diffraction. *Inorg. Chem.* **2015**, *54*, 10678–10685.
- (S14) Zhu, Z.; Li, N.; Zhao, D.; Wang, L.; Jen, A. K.-Y. Improved Efficiency and Stability of Pb/Sn Binary Perovskite Solar Cells Fabricated by Galvanic Displacement Reaction. *Adv. Energy Mater.* **2019**, *9*, 1802774.
- (S15) Kumar, M. H.; Dharani, S.; Leong, W. L.; Boix, P. P.; Prabhakar, R. R.; Baikie, T.; Shi, C.; Ding, H.; Ramesh, R.; Asta, M.; Graetzel, M.; Mhaisalkar, S. G.; Mathews, N. Lead-Free Halide Perovskite Solar Cells With High Photocurrents Realized Through Vacancy Modulation. *Adv. Mater.* **2014**, *26*, 7122–7127.
- (S16) Shi, T.; Zhang, H.-S.; Meng, W.; Teng, Q.; Liu, M.; Yang, X.; Yan, Y.; Yip, H.-L.; Zhao, Y.-J. Effects of Organic Cations on the Defect Physics of Tin Halide Perovskites. *J. Mater. Chem. A* **2017**, *5*, 15124–15129.
- (S17) Jena, A. K.; Kulkarni, A.; Sanehira, Y.; Ikegami, M.; Miyasaka, T. Stabilization of  $\alpha$ -CsPbI<sub>3</sub> in Ambient Room Temperature Conditions by Incorporating Eu into CsPbI<sub>3</sub>. *Chem. Mater.* **2018**, *30*, 6668–6674.

- (S18) Zhou, Y.; Zhao, Y. Chemical Stability and Instability of Inorganic Halide Perovskites. *Energy Environ. Sci.* **2019**, *12*, 1495–1511.
- (S19) Anaya, M.; Correa-Baena, J. P.; Lozano, G.; Saliba, M.; Anguita, P.; Roose, B.; Abate, A.; Steiner, U.; Grätzel, M.; Calvo, M. E.; Hagfeldt, A.; Míguez, H. Optical Analysis of  $\text{CH}_3\text{NH}_3\text{Sn}_x\text{Pb}_{1-x}\text{I}_3$  Absorbers: a Roadmap for Perovskite-on-Perovskite Tandem Solar Cells. *J. Mater. Chem. A* **2016**, *4*, 11214–11221.
- (S20) Zong, Y.; Wang, N.; Zhang, L.; Ju, M.-G.; Zeng, X. C.; Sun, X. W.; Zhou, Y.; Padture, N. P. Homogenous Alloys of Formamidinium Lead Triiodide and Cesium Tin Triiodide for Efficient Ideal-Bandgap Perovskite Solar Cells. *Angew. Chem., Int. Ed.* **2017**, *56*, 12658–12662.
- (S21) Nienhuys, H.-K.; Sundström, V. Intrinsic Complications in the Analysis of Optical-Pump, Terahertz Probe Experiments. *Phys. Rev. B* **2005**, *71*, 235110.
- (S22) Lloyd-Hughes, J.; Jeon, T.-I. A Review of the Terahertz Conductivity of Bulk and Nano-Materials. *J. Infrared, Millimeter, Terahertz Waves* **2012**, *33*, 871–925.
- (S23) Wehrenfennig, C.; Liu, M.; Snaith, H. J.; Johnston, M. B.; Herz, L. M. Charge-Carrier Dynamics in Vapour-Deposited Films of the Organolead Halide Perovskite  $\text{CH}_3\text{NH}_3\text{PbI}_{3-x}\text{Cl}_x$ . *Energy Environ. Sci.* **2014**, *7*, 2269–2275.
- (S24) Wehrenfennig, C.; Eperon, G. E.; Johnston, M. B.; Snaith, H. J.; Herz, L. M. High Charge Carrier Mobilities and Lifetimes in Organolead Trihalide Perovskites. *Adv. Mater.* **2014**, *26*, 1584–1589.
- (S25) Milot, R. L.; Klug, M. T.; Davies, C. L.; Wang, Z.; Kraus, H.; Snaith, H. J.; Johnston, M. B.; Herz, L. M. The Effects of Doping Density and Temperature on the Optoelectronic Properties of Formamidinium Tin Triiodide Thin Films. *Adv. Mater.* **2018**, *30*, 1804506.
- (S26) Tiwana, P.; Parkinson, P.; Johnston, M. B.; Snaith, H. J.; Herz, L. M. Ultrafast Terahertz Conductivity Dynamics in Mesoporous  $\text{TiO}_2$ : Influence of Dye Sensitization and Surface Treatment in Solid-State Dye-Sensitized Solar Cells. *J. Phys. Chem. C* **2010**, *114*, 1365–1371.

- (S27) Ulatowski, A. M.; Herz, L. M.; Johnston, M. B. Terahertz Conductivity Analysis for Highly Doped Thin-Film Semiconductors. *Submitted*
- (S28) Klug, M. T.; Milot, R. L.; Patel, J. B.; Green, T.; Sansom, H. C.; Farrar, M. D.; Ramadan, A. J.; Martani, S.; Wang, Z.; Wenger, B.; Ball, J. M.; Langshaw, L.; Petrozza, A.; Johnston, M. B.; Herz, L. M.; Snaith, H. J. Metal Composition Influences Optoelectronic Quality in Mixed-Metal Lead–Tin Triiodide Perovskite Solar Absorbers. *Energy Environ. Sci.* **2020**, –.
- (S29) Ulatowski, A. M.; Wright, A. D.; Wenger, B.; Buizza, L. R.; Motti, S. G.; Eggimann, H. J.; Savill, K. J.; Borchert, J.; Snaith, H. J.; Johnston, M. B., et al. Charge-Carrier Trapping Dynamics in Bismuth-Doped Thin Films of MAPbBr<sub>3</sub> Perovskite. *J. Phys. Chem. Lett.* **2020**,
- (S30) La-o vorakiat, C.; Cheng, L.; Salim, T.; Marcus, R. A.; Michel-Beyerle, M. E.; Lam, Y. M.; Chia, E. E. Phonon Features in Terahertz Photoconductivity Spectra due to Data Analysis Artifact: A Case Study on Organometallic Halide Perovskites. *Appl. Phys. Lett.* **2017**, *110*.
- (S31) Parrott, E. S.; Green, T.; Milot, R. L.; Johnston, M. B.; Snaith, H. J.; Herz, L. M. Interplay of Structural and Optoelectronic Properties in Formamidinium Mixed Tin–Lead Triiodide Perovskites. *Adv. Funct. Mater.* **2018**, *28*, 1802803.
- (S32) Milot, R. L.; Eperon, G. E.; Green, T.; Snaith, H. J.; Johnston, M. B.; Herz, L. M. Radiative Monomolecular Recombination Boosts Amplified Spontaneous Emission in HC(NH<sub>2</sub>)<sub>2</sub>SnI<sub>3</sub> Perovskite Films. *J. Phys. Chem. Lett.* **2016**, *7*, 4178–4184.
- (S33) Herz, L. M. Charge-Carrier Dynamics in Organic-Inorganic Metal Halide Perovskites. *Ann. Rev. Phys. Chem.* **2016**, *67*, 65–89.
- (S34) Stranks, S. D.; Eperon, G. E.; Grancini, G.; Menelaou, C.; Alcocer, M. J. P.; Leijtens, T.; Herz, L. M.; Petrozza, A.; Snaith, H. J. Electron-Hole Diffusion Lengths Exceeding 1 Micrometer in an Organometal Trihalide Perovskite Absorber. *Science* **2013**, *342*, 341–344.

- (S35) Eperon, G. E.; Stranks, S. D.; Menelaou, C.; Johnston, M. B.; Herz, L. M.; Snaith, H. J. Formamidinium Lead trihalide: a Broadly Tunable Perovskite for Efficient Planar Heterojunction Solar Cells. *Energy & Environmental Science* **2014**, *7*, 982–988.
- (S36) de Quilettes, D. W.; Vorpahl, S. M.; Stranks, S. D.; Nagaoka, H.; Eperon, G. E.; Ziffer, M. E.; Snaith, H. J.; Ginger, D. S. Impact of Microstructure on Local Carrier Lifetime in Perovskite Solar Cells. *Science* **2015**, *348*, 683–686.
- (S37) Pydzińska-Białek, K.; Szeremeta, J.; Wojciechowski, K.; Ziólek, M. Insights into the Femtosecond to Nanosecond Charge Carrier Kinetics in Perovskite Materials for Solar Cells. *J. Phys. Chem. C* **2019**, *123*, 110–119.
- (S38) Tauc, J.; Grigorovici, R.; Vancu, A. Optical Properties and Electronic Structure of Amorphous Germanium. *Phys. Status Solidi B* **1966**, *15*, 627–637.
- (S39) Elliott, R. Intensity of Optical Absorption by Excitons. *Phys. Rev.* **1957**, *108*, 1384.
- (S40) Hill, R.; Richardson, D. A Comparison of the EPM and DM Methods for Calculations in Mixed Zincblende Alloys. *J. Phys C: Solid State Phys.* **1971**, *4*, L339.
- (S41) Vurgaftman, I.; Meyer, J. R.; Ram-Mohan, L. R. Band Parameters for III–V Compound Semiconductors and their Alloys. *J. Appl. Phys.* **2001**, *89*, 5815–5875.
- (S42) Rajagopal, A.; Stoddard, R. J.; Hillhouse, H.; Jen, A. K. Y. On Understanding Bandgap Bowing and Optoelectronic Quality in Pb-Sn Alloy Hybrid Perovskites. *J. Mater. Chem. A* **2019**, *7*, 16285–16293.
- (S43) Cardona, M. Optical Properties of the Silver and Cuprous Halides. *Phys. Rev.* **1963**, *129*, 69.
- (S44) Van Vechten, J. A.; Bergstresser, T. K. Electronic Structures of Semiconductor Alloys. *Phys. Rev. B* **1970**, *1*, 3351.
- (S45) Zunger, A.; Jaffe, J. Structural Origin of Optical Bowing in Semiconductor Alloys. *Phys. Rev. Lett.* **1983**, *51*, 662.

- (S46) Bernard, J. E.; Zunger, A. Electronic Structure of ZnS, ZnSe, ZnTe, and their Pseudobinary Alloys. *Phys. Rev. B* **1987**, *36*, 3199.
- (S47) Schnohr, C. Compound Semiconductor Alloys: From Atomic-Scale Structure to Bandgap Bowing. *Appl. Phys. Rev.* **2015**, *2*, 031304.
- (S48) Thompson, A.; Woolley, J. Energy-Gap Variation in Mixed III–V Alloys. *Can. J. Phys.* **1967**, *45*, 255–261.
- (S49) Burstein, E. Anomalous Optical Absorption Limit in InSb. *Phys. Rev.* **1954**, *93*, 632.
- (S50) Moss, T. S. The Interpretation of the Properties of Indium Antimonide. *Proc. Phys. Soc., Sect. B* **1954**, *67*, 775–782.
- (S51) Handa, T.; Yamada, T.; Kubota, H.; Ise, S.; Miyamoto, Y.; Kanemitsu, Y. Photocarrier Recombination and Injection Dynamics in Long-Term Stable Lead-Free  $\text{CH}_3\text{NH}_3\text{SnI}_3$  Perovskite Thin Films and Solar Cells. *J. Phys. Chem. C* **2017**, *121*, 16158–16165.
- (S52) Yang, Z.; Zhang, X.; Yang, W.; Eperon, G. E.; Ginger, D. S. Tin-lead Alloying for Efficient and Stable All-inorganic Perovskite Solar Cells. *Chem. Mater.* **2020**, *32*, 2782–2794.
- (S53) Subedi, B.; Li, C.; Junda, M. M.; Song, Z.; Yan, Y.; Podraza, N. J. Effects of Intrinsic and Atmospherically Induced Defects in Narrow Bandgap  $(\text{FASnI}_3)_x(\text{MAPbI}_3)_{1-x}$  Perovskite Films and Solar Cells. *J. Chem. Phys.* **2020**, *152*, 064705.
- (S54) Grundmann, M. *Physics of Semiconductors*; Springer, 2010; Vol. 11.
- (S55) Galkowski, K.; Mitioglu, A.; Miyata, A.; Plochocka, P.; Portugall, O.; Eperon, G. E.; Wang, J. T.-W.; Stergiopoulos, T.; Stranks, S. D.; Snaith, H. J., et al. Determination of the Exciton Binding Energy and Effective Masses for Methylammonium and Formamidinium Lead Tri-Halide Perovskite Semiconductors. *Energy Environ. Sci.* **2016**, *9*, 962–970.
- (S56) Miyata, A.; Mitioglu, A.; Plochocka, P.; Portugall, O.; Wang, J. T.-W.; Stranks, S. D.; Snaith, H. J.; Nicholas, R. J. Direct Measurement of the Exciton Binding Energy and Ef-

fective Masses for Charge Carriers in Organic–Inorganic Tri-Halide Perovskites. *Nat. Phys.* **2015**, *11*, 582–587.

(S57) D’Innocenzo, V.; Grancini, G.; Alcocer, M. J.; Kandada, A. R. S.; Stranks, S. D.; Lee, M. M.; Lanzani, G.; Snaith, H. J.; Petrozza, A. Excitons versus Free Charges in Organo-Lead Tri-Halide Perovskites. *Nat. Commun.* **2014**, *5*, 1–6.

(S58) Hilsun, C. Simple Empirical Relationship Between Mobility and Carrier Concentration. *Electron. Lett.* **1974**, *10*, 259–260.